SLAC-PUB-8968
August 2001

MONTE CARLO CALCULATION OF THE RADIATION FIELD AT AIRCRAFT ALTITUDES [1]

Stefan Roesler[2]
Stanford Linear Accelerator Center, Stanford University, Stanford, California 94309, U.S.A.
Wolfgang Heinrich
University of Siegen, D-57078 Siegen, Germany
Hans Schraube
GSF-National Research Center for Environment and Health, D-85758 Neuherberg, Germany

Abstract

Energy spectra of secondary cosmic rays are calculated for aircraft altitudes and a discrete set of solar modulation parameters and rigidity cutoff values covering all possible conditions. The calculations are based on the Monte Carlo code FLUKA and on the most recent information on the interstellar cosmic ray flux including a detailed model of solar modulation. Results are compared to a large variety of experimental data obtained on ground and aboard of aircrafts and balloons, such as neutron, proton, and muon spectra and yields of charged particles. Furthermore, particle fluence is converted into ambient dose equivalent and effective dose and the dependence of these quantities on height above sea level, solar modulation, and geographic location is studied. Finally, calculated dose equivalent is compared to results of comprehensive measurements performed aboard of aircrafts.

Submitted to Radiation Research

[1]Work supported by Department of Energy contract DE-AC03-76SF00515
[2]Present address: CERN, TIS-RP, CH-1211 Geneva 23, Switzerland

1 Introduction

The radiation field at commercial flight altitudes has a complex nature and is different from that one on ground. Its composition and strength depend on the properties of the primary cosmic ray flux and varies with altitude. The primary cosmic ray flux is modulated by solar activity and influenced by the magnetic field of the Earth. Both effects alter mainly the low energy part of the primary spectrum which, due to its large fluence, is responsible for most of the secondary particles reaching aircraft altitudes. Solar activity modulates the absolute value whereas the magnetic field of the Earth deflects particles away from the Earth causing a low-energy cutoff in the spectrum of particles entering the atmosphere. Thus, the radiation field at aircraft altitudes can be expressed as a function of three variables, height above sea level, solar modulation strength, and rigidity cutoff.

With the increasing popularity of air-travel and its revised radiation safety standards the dose received by airline personnel and frequent flyers from secondary cosmic radiation has become subject of intensive discussion. As a result, the assessment with theoretical and experimental methods arose as an indispensable necessity.

In the past, theoretical predictions of atmospheric particle fluences have been subject to large uncertainties. The primary spectrum was known only within a factor of two and the demand in computing power for three-dimensional Monte Carlo (MC) simulations made systematic studies of all aspects of the radiation field almost impossible. Most studies were based on two-dimensional calculations, which, however, cannot predict isotropically distributed quantities, such as the low-energy neutron flux, and are often application-oriented, i.e. cannot be benchmarked to the same extend as Monte Carlo particle transport codes. Recently, however, the situation has greatly improved as detailed experimental information on the primary cosmic ray spectra is now available and powerful CPU has become relatively inexpensive. In addition, results of systematic experimental studies performed aboard of aircrafts, balloons and on ground exist to which the model predictions can be compared.

First studies assessing several aspects of the radiation environment at aircraft altitudes with MC calculations can be found in the literature [1, 2, 3]. The present work supplements and extends these studies as it attempts for the first time a systematic approach with regard to comparisons to data on both fluence and dosimetric quantities and to predictions for arbitrary flight conditions. It is based on the Monte Carlo code FLUKA and a detailed environmental model including the most recent measurements of the primary cosmic ray spectrum.

Earlier FLUKA calculations served as the theoretical basis for the European Computer Program Package for the Calculation of Aviation Route Doses (EPCARD) [4, 5]. These calculations could not yet take into account the most recent experimental information on the galactic cosmic ray spectra. Differences between the results of these earlier and the present calculations are discussed below.

2 The FLUKA-Code

FLUKA is a multipurpose particle interaction and transport program with applications as diverse as proton and electron accelerator shielding, calorimetry, medical physics, beam design, high and low energy dosimetry, isotope production, etc. [6, 7, 8]. Recently, it has also been used successfully in space and cosmic ray studies [3, 1, 9, 10, 11, 12, 13, 14, 15].

In FLUKA, different physical models, or event generators, are responsible for the various aspects of particle production at different energies. These theoretical models have been directly tested against a large amount of nuclear experimental data, and have also been indirectly validated by comparisons with shower measurements, obtained both at accelerators [16, 17, 18]

and in cosmic ray experiments [19, 18, 1, 20, 21].

For the present calculations, the following models for nuclear interactions are relevant (more details can be found in [17]):

- Hadronic interactions above 4 GeV are simulated according to the Dual Parton Model
- A cascade pre-equilibrium model is used for hadronic interactions below 3 GeV. The model includes pion and kaon production. Between 3 and 4 GeV, inelastic hadron collisions are treated according to a resonance-decay model.
- The de-excitation of nuclear fragments is treated in detail by models for evaporation, fragmentation and γ-ray emission.

The simulation of the electromagnetic cascade is very accurate, including the Landau - Pomeranchuk - Migdal effect and the sampling of electron pairs and bremsstrahlung from the proper double differential energy-angular distributions. In a similar way, the three-dimensional shape of the hadronic cascades is reproduced in detail by a rigorous sampling of correlated energy and angles in decay, scattering, and multiple Coulomb scattering. The transport of low-energy neutrons ($E < 19.6$ MeV) is based on ENEA multigroup cross-sections (72 groups) [22] with photon and fission neutron generation.

3 Details of the Calculations

Earlier studies using the 1995 version of FLUKA were discussed in detail in [1]. The present calculations differ in the following aspects

- The spectra of primary cosmic ray particles used as input to the calculations have been revised based on a large amount of direct measurements which have become available during the past years. These new spectra reduce the corresponding uncertainties in the predictions from a factor of two in the earlier study to about 25%.
- Solar modulation is treated based on a diffusion-convection model instead of a sinusoidal fit to neutron monitor count-rates. The modulation parameter of the diffusion-convection model is determined from Climax neutron monitor count-rates.
- Variance reduction techniques were applied in the simulation in order to accelerate the convergence of the results allowing to calculate particle spectra at all heights with comparable statistical significance.
- Thermal neutrons were included in the FLUKA calculations.
- In addition to the hadronic cascade also the full electromagnetic cascade was simulated in detail.
- The latest version of FLUKA (FLUKA99) was used. The code is rapidly evolving. Changes since FLUKA95 include the extension of the cascade pre-equilibrium model in energy from 1 GeV to 3 GeV, a new implementation of diffractive hadronic interactions, a largely revised evaporation model and the transport of nuclear fragments.

The following discussion details these new aspects.

3.1 The Spectra of Galactic Cosmic Rays

As will be shown later more than 80% of the dose at aircraft altitudes is caused by primary cosmic rays with energies below 100 GeV. In this energy range data from several independent direct measurements of the proton and helium spectra exist which were obtained with balloon-borne spectrometers [23, 24, 25, 26]. More recently, spectra measured with the AMS detector on the Space Shuttle [27, 28] have also become available. At higher energies further direct and indirect measurements have provided information on the primary spectra which approximately follow a $E^{-\alpha}$-behavior with a constant exponent α up to about 1000 TeV / nucleus. Compilations of these high-energy data as well as parameter-fits can be found, for example, in Refs. [29, 30].

Fig. 1 shows a summary of measured primary proton and helium spectra. All data were multiplied by $E^{2.7}$ in order to emphasize the spectral shape above 50 GeV / n which is not affected by solar modulation. As can be seen, the experimental data are consistent with each other and with the high-energy fits within approximately 25% for protons and 50% for helium. The primary spectra used in the present calculations are shown in Fig. 1 as solid curves. They are based on spectra by Badhwar [33] which were scaled to match the recent experimental data.[3] The spectra of heavier cosmic ray nuclei were also obtained from [33].

Solar modulation of the primary spectra is described in the framework of a diffusion-convection model [33]. Within this model the modulation strength at a time T is controlled by a single parameter Φ (in MV), the so-called deceleration potential. This parameter is assumed to depend linearly on the Climax neutron-monitor count rate C (prescaled by 100) at time $T' = T - 95$ days, averaged over $T' \pm 14$ days [33]:

$$\begin{aligned} \text{Positive field}: &\quad \Phi(T) = 3957.89 - 0.8124\ \langle C(T')\rangle_{\pm 14\ \text{days}} \\ \text{Negative field}: &\quad \Phi(T) = 4202.76 - 0.8563\ \langle C(T')\rangle_{\pm 14\ \text{days}} \\ \text{Field reversal}: &\quad \Phi(T) = 4772.86 - 0.9528\ \langle C(T')\rangle_{\pm 14\ \text{days}} \end{aligned} \tag{1}$$

The above relations account for a time-lag of 95 days. The time-lag reflects the response of Climax – due to its location – to only relatively high energy primary cosmic rays with rigidities above about 3 GV. The information on solar activity is carried to the solar modulation boundary at about 100 AU by the solar wind. High energy particles having sensed a change in modulation at these large distances arrive first at 1 AU. Therefore, this time-lag allows to predict primary spectra up to 95 ± 14 days in advance. Furthermore, changes in the polarity of the heliospheric magnetic field which occur about every 11 years are taken into account by different relations for the different field conditions. Fig. 2 shows the Climax count rate [35][4] and the corresponding values of the solar modulation parameter for the past fifty years. Periods of different field polarity are indicated by dotted lines.

Solar modulation affects the low energy part of the primary spectra for which data from balloon-borne and Space Shuttle measurements exist. Table 1 summarizes dates and locations of these measurements. In addition, the corresponding modulation parameters as obtained from the Climax count-rates for the respective dates and Eq.(1) are given. The measurements cover the whole range of solar modulation parameters and thus provide a valuable check on the modulation model. Fig. 3 shows the measured proton and helium spectra together with the spectra used in this work modulated with the parameters listed in Table 1. The spectra are multiplied by E^2 so that equal areas on a semilogarithmic plot correspond to equal contributions to the energy content of cosmic radiation. Whereas good agreement is found for the IMAX-

[3] Recently, Badhwar *et al.* have provided us with updated spectra [34] which are essentially in agreement with those used in the calculations.

[4] The University of Chicago, "National Science Foundation Grant ATM-9912341 is acknowledged.

and CAPRICE-data the proton spectrum measured by MASS is underestimated by up to 30% below 20 GeV. This disagreement may indicate uncertainties associated with the time-lag and with averaging the Climax count rates over ± 14 days during periods of rapidly changing modulation as was the case in 1991. Similar arguments might explain the slight underestimation of the BESS-data. Due to the time-lag of 95 days, the drop in the neutron monitor count rates at the end of April 1998 results in an increase of the modulation potential for the end of July 1998 when the BESS-data were taken. The measurements of AMS and BESS however indicate similar modulation conditions from June until the end of July 1998 which could suggest a larger time-lag.

The geomagnetic field acts as a shield against low-energy primary protons and nuclei. The rigidity cutoff below which protons and nuclei are deflected such that they are not able to enter the atmosphere depends on the location and direction of incidence on top of the atmosphere. The cutoff for vertical incidence is obtained from an one-by-one degree world grid of trajectory-determined cutoffs [36, 37]. These cutoffs are based on the 1990 International Geomagnetic Reference Field. Values range from zero at the geomagnetic poles to 17.6 GV at the geomagnetic equator. A dipole model of the Earth's magnetic field is used to correct these cutoffs for non-vertical directions (see [1] for further details). Fig. 4 shows the total nucleon spectrum for a solar modulation parameter of 465 MV, i.e. close to solar minimum, and different vertical rigidity cutoffs. Note, that the rigidity cutoff translates into an kinetic energy cutoff which depends on the charge-to-mass ratio of the primary. This results in lower cutoffs for nuclei than for protons explaining the two-component structure in the nucleon spectra close to cutoff. In addition a spectrum for solar maximum and zero cutoff is shown. As can be expected already from this figure, the higher the rigidity cutoff is the lower is the effect of solar modulation on the radiation field in the atmosphere.

The unmodulated primary spectra, the solar modulation model [38], and the rigidity cutoff treatment are implemented in a "user-routine" of FLUKA. It allows to specify geographic location and date (or, optionally, vertical rigidity cutoff and modulation parameter) directly in the input-file of the simulation. Based on this information the distributions from which primary particles are sampled are calculated by FLUKA in an initialization step.

3.2 Parameters and Simulation Strategies

The atmosphere is approximated by 50 layers, each of uniform average density. The density between different layers is exponentially decreasing with altitude according to a standard atmospheric density profile (see discussion in [1]). All hadrons except neutrons were transported down to 1 MeV. Neutrons were followed down to thermal energies. The transport threshold for photons and electrons were set at 10 keV and 100 keV, respectively.

In order to avoid large fluctuations in the results due to the steeply decreasing primary spectrum stratified sampling was applied in the following way. The energy range of the primary spectrum between cutoff and 15 TeV was split into five intervals with boundaries of 50 GeV, 200 GeV, 1 TeV and 5 TeV. Separate FLUKA simulations were performed for each of the five intervals and results were added subsequently. As solar modulation and geomagnetic field affect the spectra only below 50 GeV this strategy allowed to use the results above that energy for any rigidity cutoff and modulation parameters. Only the simulations for the first interval had to be repeated for different cutoff and modulation conditions. Within each interval the energy was sampled uniformly and the fluence was taken into account by assigning a corresponding weight to the primary particle.

In FLUKA, as in most Monte Carlo codes used to solve deep penetration problems, several variance reduction techniques, so-called "biasing" options, are available in order to accelerate

the convergence of the results in phase space regions in which it would otherwise be difficult to achieve reasonable statistical significance. Rigorous proofs of the convergence of results obtained by these techniques to the correct value can be found in specialized books [39]. In the present calculations, two biasing options have been used:

- Leading particle biasing: At each electromagnetic interaction with two particles in the final state (bremsstrahlung, pair production, etc.) only one of the two particles is followed, with a probability proportional to its energy. Its statistical weight is modified so as to conserve total weight.
- Importance splitting: The loss of statistics due to decrease of particle number with depth in the atmosphere is compensated by replacing a Monte Carlo particle with additional identical particles of lower statistical weight when the particle crosses a boundary between two regions of different pre-defined statistical importance.

Since FLUKA does not include a model for nucleus-nucleus interactions the shower initiated by a primary nucleus of mass A was replaced by A individual nucleon showers ("superposition model", see also the discussion in [1]).

4 Comparison to Experimental Data

Although a variety of comparisons of FLUKA predictions to data on cosmic ray cascades exists in the literature [19, 18, 1, 20, 21] it might still be worthwhile to add a few more examples as some of them concern directly the radiation field at airplane altitudes. The examples given in this section are restricted to measurements of physical quantities, such as particle fluence. FLUKA results for dose equivalent and comparisons to experimental data will be addressed in the next section.

4.1 Neutron Spectra

4.1.1 Ground Level Spectra

The fluence of secondary cosmic ray neutrons was recorded in an experiment at the Schneefernerhaus, Germany in March 1997. The Schneefernerhaus is located below the summit of the mountain Zugspitze at an altitude of 2660 m above sea level (746 g/cm^2). The measurements were performed with a multisphere spectrometer consisting of 16 measuring channels, i.e. 12 homogeneous polyethylene spheres, 2 polyethylene spheres with internal lead converter as high energy channels and a bare ^{3}He proportional counter which is also used as thermal neutron detector in the center of each sphere (see [4, 40] for details). Twelve detectors were used to derive the spectra shown below. The detectors were housed in an aluminum box and placed on a concrete terrace outside the Schneefernerhaus 1 m above the floor. Before the measurements the terrace around the box was cleared from snow as good as possible. However, the snow on a second, lower platform just in front of the detectors was not removed.

The unfolding of the experimental count rates was done using the iterative code SANDII [41]. In contrast to the unfolding of the atmospheric spectra shown in Sect.4.1.2 [42, 43] no a priori information on the spectral structure was employed. Instead a $1/E$ distribution in the energy range from 10^{-3} to 10^{10} eV was used as first guess spectrum. Therefore, the experimental results are fully independent from the FLUKA calculations. Further details on the experiment will be published elsewhere [44].

Ground level neutron spectra depend strongly on the environmental conditions which were therefore considered in the FLUKA simulations. The geometry included a concrete layer of

50 cm thickness and a 10 cm thick layer of snow (density 0.3 g / cm^3) covering the concrete. The neutron spectrum was scored at 1 m above the concrete floor. The aluminum box was modelled by two 2 mm thick layers at 30 cm above and below the scoring location. Furthermore, atmospheric water vapor was taken into account assuming a total column water vapor of 7.5 mm [45]. In order to study the effect of the different environmental conditions on the neutron count rates a total of five FLUKA simulations was performed each using a different combination of water vapor, aluminum container, snow, and concrete floor. A summary is given in Table 2.

Fig. 5 shows the neutron spectra from the five calculations together with the measured (unfolded) spectrum. As can be seen from a comparison of the calculated spectra 1 and 3 (or 1 and 4) the concrete floor modifies the slope of the spectrum below about 100 keV and decreases the fluence in the energy range between 1 eV and approximately 1 MeV. It has practically no influence on the spectrum at higher energies. In the thermal energy range the cross section data sets used by FLUKA contain only one energy bin. Correspondingly, also the neutron fluence below 0.4 eV is represented by only one average value. This value is strongly increased by thermal neutrons back-scattered from the concrete floor.

Atmospheric water vapor and the aluminum container change the spectrum only slightly. The former decreases the low energy neutron fluence whereas the latter causes an increased fluence due to additional neutron production and scattering. The snow has the largest effect of the all the additional materials (cf. spectra 2 and 4). It significantly reduces the fluence below 10 MeV (except for the thermal neutron bin) and creates a $1/E$-shape between about 1 eV and 10 keV.

The calculations reproduce the high-energy part of the measured spectrum including the 100 MeV peak rather well. At lower energies the FLUKA calculations generally overestimate the measured spectral fluence rate. However, as the simulations showed, this part of the spectrum depends significantly on the material distribution around the detector. The disagreement might therefore be partially due to the incomplete simulation of the actual experimental setup. The enhancement in the measured spectrum around 0.1 keV is not fully understood yet. In the thermal energy range the cross section data sets used by FLUKA contain only one energy bin. Correspondingly, also the neutron fluence below 0.4 eV is represented by only one average value.

Neutron spectra determined with Bonner sphere spectrometers always depend to some extend on the assumptions entering the unfolding procedure. It may therefore be helpful to fold the calculated spectra with the response functions of the spheres and to compare measurements and calculations on a count rate basis. Table 3 gives the measured count rates together with the calculated count rates for the five simulations. The ratios of calculated and measured values are shown in Fig. 6. The calculation which models also the snow results in the best agreement with the experiment, though the calculated values are on average larger by a factor of 1.6. The slight increase of the ratio towards smaller spheres is partly due to the simplified description of the thermal neutron group.

4.1.2 Atmospheric Spectra

Probably the most comprehensive measurement of neutron spectra aboard of an airplane was performed by Goldhagen *et al.* on five supersonic flights in June 1997 [46, 42, 43]. As part of the AIR-project [46], the flights with an ER-2 high-altitude airplane were dedicated for cosmic ray measurements and covered vertical rigidity cutoffs from 0.7 GV to 11.9 GV. The airplane carried a large variety of detectors sensitive to various types of secondary cosmic radiation. Neutrons were measured with a Bonner sphere spectrometer consisting of 12 detectors. Two of these detectors contained lead and steel shells, respectively, and were therefore responding to

high-energy neutrons. Table 4 summarizes the measurement conditions.

For the unfolding of the experimental count rates the MAXED code [47] was employed by Goldhagen *et al.* which uses the Maximum Entropy Principle for deriving the spectral solution. It requires as much as physical information in defining the a priori default spectrum and retains its fine structure.

Fig. 7 shows measured and calculated spectra for three of the experimental conditions. Two of them (Fig. 7a and b) are typical altitudes of supersonic flights and locations close to the magnetic pole and to the equator. The third measurement location (Fig. 7c) is a commercial flight altitude at medium latitude. Due to the deconvolution procedure the unfolded spectra show similar spectral substructures as the calculated ones which were used as default input for the unfolding. Though the result is not independent from the input spectrum, the relative spectral components are changed to fit best to the experimental data: In all cases the neutron fluence rate in the evaporation peak at around 2 MeV is slightly increased compared with the calculated spectrum.

Table 5 gives the experimental and calculated neutron count rates for each sphere and measurement condition. The experimental values were corrected for proton- and pion-induced counts by folding calculated proton and pion spectra with the respective response functions and by subtracting these numbers from the total count rate. The ratios of calculated and measured rates are shown in Fig. 8. The agreement is within 15% for all detectors but the bare ^{3}He counter (detector 1) and the largest sphere with the embedded steel layer (detector 14) for which the count rates agree within 25%.

4.2 Ground Level Spectra of Vertical Hadrons

Though there are no direct implications for the estimation of doses to aircraft crews, the flux of high-energy hadrons at ground gives important information on the shape and absolute magnitude of the primary spectra at high energy. Furthermore, these hadrons have undergone only a few, peripheral interactions and provide a benchmark for the hadronic interaction model in air shower simulations. In particular, calculated ground level hadron spectra are sensitive to features of the model in forward direction[5] which are often not accessible with existing detectors at particle colliders. In the following only two examples are given. Although they were both already discussed in [1], the modifications in the primary spectra entering the present calculations might affect the high-energy hadron spectra at ground. In addition, the biasing techniques employed here allow calculations with much better statistical significance than has been previously possible.

Fig. 9 shows the flux of neutrons reaching sea level with polar angles with respect to the vertical of less than 15° (vertical neutrons). To allow a detailed comparison of calculated and measured spectra, the flux which drops with energy approximately as $E^{-2.7}$ (the asymptotic behavior of the primary spectra, see Fig. 1) has been multiplied by with its inverse behavior, $E^{2.7}$. A good agreement between the FLUKA results and the data obtained by the KASKADE experiment [49] is found up to about 500 GeV. At higher energies the flux is underestimated by the calculations as primary energies above 15 TeV contribute which were not taken into account in the simulations.

The vertical proton flux at an altitude of 3200 m above sea level is shown in Fig. 10. By comparing this figure to Fig. 15 of the earlier paper [1] it can be readily seen that the statistical

[5]The kinematic phase space region in a hadronic collision which is close to that one of the projectile is commonly referred to as "forward direction". If, e.g., the particle yield from a high energy hadron-nucleus collision is plotted as function of the fraction x of the projectile energy carried by the particle, the forward direction is the region of x-values close to one.

significance of the calculated results has improved significantly. In addition, the spectrum is slightly lower (due to modifications in the primary cosmic ray flux) and in good agreement with the data [50].

4.3 Atmospheric Muon Fluence and Spectra

Detailed data on the atmospheric muon flux have become available in the recent past from balloon-borne experiments. As these experiments recorded both primary cosmic ray spectra and muon spectra their data provide further valuable checks for the hadronic interaction models of air shower simulations.

Fig. 11 shows the flux of positive and negative muons for different intervals in the muon momentum as function of depth in the atmosphere. FLUKA results are compared to data obtained with the CAPRICE spectrometer [51]. Corresponding to the average geometrical response of the CAPRICE apparatus only muons with a polar angle with respect to the vertical of less than 9° (vertical muons) were scored in the simulations. As can be seen from the figure, FLUKA provides a good description of the muon flux from the top of the atmosphere down to sea level and for all momentum intervals.

Energy spectra of muons were measured with the CAPRICE spectrometer also at ground, at an atmospheric depth of 886 g/cm^2 [52]. These spectra are compared to FLUKA results in Fig. 12a. Note, that the spectra are given as function of the muon momentum p and are multiplied by $p^{2.5}$ to emphasize the high-energy part. Again, good agreement between simulations and experiment is found.

Finally, Fig. 12b shows the ratio of the yields of positive and negative muons as function of the muon energy. The FLUKA results reproduce well the ratios and follow the measured energy dependence [52] though the statistical uncertainty in the latter is considerable.

4.4 Charged Particle Yields at Aircraft Altitudes

Ionizing radiation was measured with the DOSTEL dosimeter on nine commercial flights between July 1996 and February 1997 [53, 54]. The flights connected Germany with both North- and South-American destinations and thus covered a wide range of latitudes. The period was characterized by stable solar minimum conditions with modulation parameters ranging from 490 MV to 520 MV. The DOSTEL instrument consists of two planar silicon detectors and measures count and dose rates as well as LET spectra of ionizing radiation. During the flights is was located on the flight deck of the aircrafts.

Fig. 13a compares the count rates measured during two of the flights (San Francisco - Frankfurt and Rio de Janeiro - Frankfurt) with the calculated current of charged particles passing through a horizontal plane. As detailed flight information was available the comparison could be performed for the same conditions (latitude, longitude, altitude, and date). The data are shown as a function of the elapsed time after take-off. To reduce statistical fluctuations within the measured count rates, periods of rapidly changing altitude, e.g. immediately after take-off and before landing and during changes of the flight level, were eliminated and data were averaged over 5 minutes [54].

The ratio of calculated current and measured count rate is shown for all nine flights in Fig. 13b. The graph shows the ratios as function of the vertical rigidity cutoff. Calculated and measured values deviate from each other by less than 15% with most of the ratios being between 0.9 and 1.0. In addition, a systematic drop of the ratios with increasing cutoff is observed. The fact that the measured rates were not corrected for the response of the detector to photons and neutrons [54] might explain the underestimation, though would not explain the

systematic decrease. However, considering the uncertainties in both calculations and measurements the agreement is surprisingly good.

Experimental data on ionizing radiation at aircraft altitudes exist also for the previous solar minimum period and for large rigidity cutoffs. The experiment [55] was carried out in June 1989 with the VEGA-detector, a lead-glass-based electron telescope, aboard of a cargo airplane on a flight from Narita (Japan) to Sydney (Australia). Rigidity cutoffs covered by this flight range from 5.0 GV to 16.2 GV. The detector measured vertically incident charged particles within a cone of 15° and allowed to discriminate electrons, which are the major contributors to the ionizing radiation.

Due to the narrow acceptance cone of the detector the FLUKA simulations were rather time-consuming and could only be carried out for a few selected rigidity cutoff values. Correspondingly, only experimental results obtained close to these cutoff values were considered in the comparison. Fig. 14 shows the experimental results for cutoff intervals from 5.0 GV to 6.8 GV and from 15.4 GV to 16.2 GV together with the FLUKA results for the discrete cutoffs of 5.9 GV and 15.9 GV, respectively. For either interval the comparisons are shown for different lower electron energy cutoffs. The range of depths covered by the graph (200-300 g / cm^2) corresponds to altitudes from about 9.3 to 11.9 km. As can be seen from the figure, experimental data are again well reproduced by the calculations.

5 Radiation Fields and Doses at Aircraft Altitudes

5.1 Particle Fluence Rates and Spectra

With the aim of calculating the dose equivalent accumulated on arbitrary flight routes FLUKA-simulations were performed for a set of solar modulation parameters and vertical rigidity cutoffs which covered all possible values of each variable. The solar modulation parameter Φ was chosen to be 465, 700, 900, 1100, 1300, and 1500 MV. For $\Phi = 465$ MV the particle cascades were calculated for a total of nine different cutoffs (0, 1, 2, 3, 4, 5, 10, 15, and 17 GV) and for all other modulation parameters for a total of four cutoffs (0, 4, 10, and 17 GV). The finer mesh for 465 MV allowed also a more precise interpolation in cutoff at the other modulation parameters. For each of the 29 combinations of modulation and cutoff parameter the fluence spectra of neutrons, protons, positively and negatively charged pions, muons, photons, electrons and positrons were calculated for 36 heights above sea level from ground level to the top of the atmosphere.

Fig. 15a shows an example for the energy spectra, here given for $\Phi = 465$ MV, zero rigidity cutoff, and a height above sea level of 10580 m which is one of the scoring altitudes in the FLUKA-simulations. The error bars reflect the statistical uncertainties of the calculations. The total, energy integrated fluence for altitudes between 2 km and 16 km is shown in Fig. 15b. The total fluence is dominated by photons, followed by neutrons, electrons, and positrons. As compared to neutrons or electromagnetic particles the proton fluence decreases much stronger with height and the muon fluence drops only slowly.

5.2 Conversion of Fluence to Dose Equivalent

Ambient dose equivalent and effective dose were obtained by folding the fluence spectra with energy-dependent conversion coefficients [56]. In case of effective dose they are based on the radiation weighting factors recommended in ICRP Publication 60 [57]. In the following, the effective dose coefficients for an isotropic irradiation geometry were used which most closely resembles the situation in an aircraft. As an example, Fig. 16a shows the conversion coefficients

for neutrons and protons. At energies above 50 MeV the values for ambient dose equivalent (dashed lines) are well below those for effective dose (solid lines) indicating that ambient dose equivalent might not always provide a conservative estimate of effective dose in an environment where high energy hadrons contribute significantly to the total dose.

The result of multiplying the neutron and proton spectra of Fig. 15a with these conversion coefficients is shown in Figs. 16b and c, respectively. In case of neutrons the 1 MeV-peak in the spectrum contributes more than 50% to the ambient dose equivalent whereas high energy neutrons dominate effective dose. The effective dose by protons is clearly larger than the corresponding ambient dose equivalent.

Energy-averaged conversion coefficients are obtained by integrating the fluence and dose spectra (such as those in Figs. 15a and 16b) and by calculating the ratio of the two values. This ratio, e.g. plotted as function of altitude, should reveal possible changes in the spectral shape. Fig. 17 shows the average conversion coefficients for neutrons, protons, and electrons / positrons and for zero and maximum rigidity cutoff. Note, that in order to display the proton-coefficients on the same scale the values for effective dose were scaled down by a factor of 3. As expected, there is in general only a weak dependence with height. For flight altitudes the values vary only within about 15% showing the strongest dependence for effective dose by neutrons (17 GV cutoff) and by electrons (both cutoffs). The average conversion coefficients for effective dose are lower than those for ambient dose equivalent for both neutrons and electrons. However, they are larger by more than a factor of 3 for protons which is mainly due to the radiation weighting factor of 5 recommended by ICRP [57].

5.3 Calculation of Route Doses

Doses for arbitrary flight routes were obtained by a 3-dimensional interpolation in height, solar modulation, and cutoff based on the results for the above mentioned 29 combinations of modulation parameter and rigidity cutoff. The interpolation was implemented as a FORTRAN-routine which returns fluence, effective dose or ambient dose equivalent for each particle type and for a certain set of input parameters. These parameters can be either height, modulation, and cutoff directly or, more conveniently, flight level, date, and geographic latitude and longitude.

5.3.1 General Properties

In the following, general properties of the radiation field are discussed in terms of ambient dose equivalent which is also the quantity typically reported by dosimetry experiments performed aboard of aircrafts. This is justified as part of the experimental devices effectively measure particle fluence rate weighted by their energy-dependent response. However, most of the conclusions from results presented in this section would also apply to effective dose.

Fig. 18a shows the dose rate as function of rigidity cutoff for the different particle types, an altitude of 10 km, and a solar modulation of 400 MV. Below 9 GV more than half of the total dose is due to neutrons with the contribution from electrons and positrons increasing at larger cutoffs. Protons cause less than 15% to the total ambient dose equivalent but would contribute significantly to effective dose (see, for example, [3, 5]).

The cutoff-dependence of the total dose rate is shown for different modulation parameters and fixed altitude (10 km) and for different altitudes and fixed solar modulation (400 MV) in Figs. 18b and c, respectively. Solar modulation affects only locations of small rigidity cutoff and may cause up to a factor of two increase in dose from solar maximum to solar minimum. On

the other hand, altitude has a more pronounced effect on the dose rates. For example, the dose at an altitude of 12 km is up to a factor of 3 higher than the dose at an altitude of 8 km.

The contribution of primary cosmic ray particles with rigidities below a certain value to the total dose at aircraft altitudes can be estimated from the the curves shown in Fig. 18. For example, if D_1 and D_2 are the dose rates for a certain altitude and modulation parameter and for two locations with rigidity cutoffs $R_{\mathrm{V}1}$ and $R_{\mathrm{V}2}$ ($R_{\mathrm{V}1} < R_{\mathrm{V}2}$), then $D_1 - D_2$ is the dose rate caused by particles with rigidities R between $R_{\mathrm{V}1}$ and $R_{\mathrm{V}2}$.

Fig. 19 shows this distribution function for the geomagnetic pol, a solar modulation of 400 MV, four different altitudes and for all particles (a), neutrons (b), and charged particles (c). For example, at an altitude of 10 km about 12% of the total ambient dose equivalent is caused by primary particles with rigidities below about 2 GV (i.e. energies below about $1 - 2$ GeV, cf. Fig. 4), 50% by particles with rigidities below about 6 GV, and 80% by particles with rigidities below 18 GV. These rigidity values are lower for dose from neutrons and somewhat higher for dose from charged particles. Hence, the ambient dose equivalent at aircraft altitudes and high latitudes (low rigidity cutoffs) is mainly caused by primary particles with energies below ~ 20 GeV and an accurate description of the primary spectrum at low energies is particularly important. Of course, the situation becomes somewhat different at lower latitudes and correspondingly larger rigidity cutoff values for which those functions could be calculated in a similar way.

5.3.2 Comparison to Dose Measurements

A series of measurements of ambient dose equivalent was performed aboard of cargo airplanes between May 1997 and February 1999 within the ACREM project [58]. Several dosimeters sensitive to both neutrons and ionizing radiation were flown on a total of 39 flight legs covering the whole range of rigidity cutoff values. For each flight the dose rates measured by the different devices were recorded as function of the time after take-off together with detailed information on flight level, latitude, and longitude [59] which allowed a comparison to calculated dose rates for the same conditions. In the following, the FLUKA results for ambient dose equivalent from neutrons and from other particles (i.e. total dose minus neutron dose) are compared to the dose readings of a lead-modified Andersson and Braun rem counter (neutrons) and of a high pressure ionisation chamber (ionizing component), respectively.

The ambient dose equivalent rate is shown for two selected flights as function of the elapsed time after take-off in Fig. 20. The flight from Frankfurt to Fairbanks is a polar route and therefore characterized by small rigidity cutoff values whereas the flight Frankfurt-Sao Paulo (with stopover in Dakar) crosses the equator and is typical for a low-latitude (high rigidity cutoff) flight. The measured neutron dose rate (Fig. 20a) is overestimated by the calculations for the polar route but agrees relatively well with the FLUKA results for the flight to Sao Paulo. The ionizing component is slightly underestimated for both flights.

The total ambient dose equivalent rate for all flights is given as function of the rigidity cutoff in Fig. 21. Here, the experimental values are normalized to an altitude of 10.6 km and a solar modulation parameter of 650 MV using the calculated altitude and modulation dependence of the dose. As the figure shows, the calculations predict slightly higher doses at small cutoffs whereas underestimate the measured doses at higher cutoffs. The magnitude of the discrepancy can be more clearly seen from the ratios of calculated and measured dose rates in Fig. 22, here given separately for neutrons and for the ionizing component. In both cases the ratios are cutoff-dependent, more pronounced for neutrons than for the ionizing component. Despite these differences the agreement between calculations and measurements is encouraging taking into account the uncertainties in the response of the instruments to the particle composition

and spectra at flight altitudes, the effect of the aircraft on the doses (not taken into account in the calculations), uncertainties in the actual solar modulation at the date of the flight, etc.

A similar experimental study [60] was performed with a tissue-equivalent proportional counter (TEPC) on a series of commercial flights in 1999. Again, detailed flight information was available [61] and each data point could be normalized to an altitude of 10.6 km and a modulation parameter of 650 MV using the calculated dependencies from the two variables. Fig. 23 shows the resulting values as function of the rigidity cutoff together with the FLUKA prediction (same curve as in Fig. 21). Except for larger statistical fluctuations the TEPC data are consistent with the above Andersson and Braun measurements and therefore similar conclusions also apply here.

Data from in-flight dose measurements exist also for the last solar maximum period. In particular, ambient dose equivalent was recorded with a lead-modified Andersson and Braun rem counter [62] of the same construction as above, on five flights during the period from May 1992 to March 1993. The flight routes included also the polar position, the equator and deep south locations. Corrections were applied to the instrument readings to allow for the different response due to different spectra and radiation incidence during calibration and measurement, respectively. For the calibration situation the spectrum of an AmBe-radionuclide source was used, and for the situation in the airplane the calculated neutron spectrum at 11.6 km altitude. Changes in spectral shape with altitude and cutoff, and the response to protons were not yet taken into account. Fig. 24a shows the data for two of the flights as function of the elapsed time after take-off together with FLUKA results. The first flight (Seattle-Hamburg) is typical for a flight at high latitudes and small rigidity cutoffs whereas the second flight (Frankfurt-Johannesburg) is covering a wide range of medium and large cutoffs. As can be seen from the figure, the measured doses for both flights are well described by the calculations. The ratio of calculated and measured dose equivalent as function of the rigidity cutoff is given for all five flights in Fig. 24b. The average ratio is 1.02 ± 0.11. Unlike seen in the above comparisons, these ratios do not seem to show a significant cutoff-dependence. The ratios as calculated using the predictions of EPCARD are shown in Fig. 25. As can be seen, the predictions of EPCARD which are based on earlier FLUKA calculations [5] give slightly larger ratios (7% for the considered flights). This is due to the fact that in EPCARD the spectral shapes at flight altitudes are assumed to be constant and, thus, constant, i.e. height- and cutoff-independent conversion factors are used whereas in the present study these factors are both height- and cutoff-dependent (see, e.g., Fig. 17). Furthermore, the primary cosmic ray spectra which EPCARD is based on are slightly higher than those used in the present work.

Finally, also the ER-2 high-altitude airplane carried a TEPC for ambient dose equivalent measurements on its four scientific flights - the same flights during which also neutron energy spectra were measured (see discussion in Sec. 4.1.2). The dose equivalent data from three of the flights [63, 64] are compared with FLUKA results in Fig. 26a. As FLUKA predicts significantly lower dose rates than those which were measured, the calculated values were scaled up by a factor of 1.6 to allow a direct comparison of the dose rates profiles. The profiles are well described within the (relatively large) statistical error of the data except for the altitude dip during the northern flight which might be due to experimental uncertainties. Fig. 26b shows again the ratio of calculated and measured dose rate as function of rigidity cutoff. The discrepancy between data and FLUKA results in the overall normalization seems to be fairly cutoff-independent and is difficult to understand taking into account the excellent agreement of the calculated neutron spectra with the data of the Bonner sphere spectrometer taken on the same flights (see Sec. 4.1.2).

6 Summary and Conclusions

The hadronic and electromagnetic particle cascades caused by interactions of primary cosmic rays in the atmosphere are calculated using FLUKA. The simulations are based on a detailed model for the primary cosmic ray spectra incorporating all recent measurements performed with high-altitude balloons and aboard of the Space Shuttle.

Results are compared to a large variety of experimental data including the following:

- Neutron spectra measured at mountain altitudes: These spectra which are derived from unfolding without any a priori spectral structure show good agreement with the calculated ones if the environmental conditions around the experimental position are taken into account. The evaporation neutrons (around 2 MeV) and lower energetic neutrons are somewhat overestimated by the calculations.

- Neutron spectra measured aboard of a high-altitude aircraft: These spectra are derived from a different unfolding concept than the concept used for the spectra at the Schneefernerhaus which determines the relative spectral components in a given default spectrum. The FLUKA results are in good agreement with the data in the whole rigidity cutoff range from 0.8 GV to 11.9 GV including those data taken at commercial flight altitudes. The experimental data deliver a somewhat higher contribution due to evaporation neutrons. Generally, it appears that the relative contribution of the high energy peak (around 100 MeV) is less dominant at high altitudes than at mountain altitudes.

- Vertical hadron flux at sea level and mountain altitudes: The experimental data are well described by the simulations.

- Atmospheric muon flux: The FLUKA calculations are in excellent agreement with the CAPRICE-data from the top of the atmosphere down to sea level including the ground-level muon charge ratio.

- Current of charged particles at aircraft altitudes: The ratios of calculated and measured count rates show a slight rigidity cutoff dependence. Nevertheless, the experimental data are well described by the calculations (within 10%).

- Vertical electron flux at aircraft altitudes: Again, good agreement is found for a large range of rigidity values.

Atmospheric particle spectra are calculated with FLUKA for 29 combinations of rigidity cutoff and solar modulation covering all possible values of the two variables and for 36 altitudes from sea level to the top of the atmosphere. Based on these results the particle environment at aircraft altitudes is obtained for arbitrary location and date by interpolation.

The fluence spectra are converted into ambient dose equivalent and effective dose using energy-dependent conversion coefficients. Dose rates for commercial flight routes are calculated and compared to a large amount of data obtained by different experimental groups. The data are described within about 30%. Some of the comparisons show a rigidity cutoff dependence of the ratios of calculated and measured doses which is not yet understood.

The calculations discussed in this paper will serve as theoretical basis of the EPCARD code for the determination of route doses and replace those presently used in this code.

Acknowledgments

The authors are grateful to Keran O'Brien, Alberto Fassò, and Alfredo Ferrari for many stimulating discussions and to Rudolf Beaujean, Bernard Ellaschuk, Paul Goldhagen, J. Kopp, Brent Lewis, and Ulrich Schrewe for providing the experimental data and valuable information. The authors also thank Gautam Badhwar for providing the code for the solar modulation model. The work of S.R. was supported by the Department of Energy under contract DE-AC03-76SF00515. The work of W.H. and H.S. was supported by the European Commission under contract FI4P-CT95-0011A.

References

[1] S. Roesler, W. Heinrich and H. Schraube, Calculation of radiation fields in the atmosphere and comparison to experimental data. *Radiat. Res.* **149**, 87-97 (1998).

[2] I. A. Kurochkin, B. Wiegel and B. R. L. Siebert, Study of the radiation environment caused by galactic cismic rays at flight altitudes, at the summit of the Zugspitze and at PTB Braunschweig. *Radiat. Prot. Dosim.* **83**, 281-291 (1999).

[3] A. Ferrari, M. Pelliccioni and T. Rancati, Calculation of the radiation environment caused by galactic cosmic rays for determining air crew exposure. *Radiat. Prot. Dosim.* **93**, 101-114 (2001).

[4] H. Schraube, V. Mares, S. Roesler and W. Heinrich, Experimental verification and calculation of aviation route doses. *Radiat. Prot. Dosim.* **86**, 309-315 (1999).

[5] H. Schraube, W. Heinrich, G. Leuthold, V. Mares and S. Roesler, Aviation Route Dose Calculation and its Numerical Basis. In *Proceedings of the Tenth International Congress of the International Radiation Protection Association (IRPA-10)*, Hiroshima, Japan, 2000. Available from `http://www.oita-nhs.ac.jp/\%7Eirpa10/CD-ROM/Full/t4.html`.

[6] A. Fassò, A. Ferrari, J. Ranft and P. R. Sala, New Developments in FLUKA modeling of hadronic and EM interactions. In *Proceedings of The Third Workshop on Simulating Accelerator Radiation Environments (SARE-3)* (H. Hirayama, Ed.), pp. 32-43. Proceedings 97-5, KEK, Tsukuba, Japan, 1997.

[7] A. Fassò, A. Ferrari and P. R. Sala, Electron-photon transport in FLUKA: Status. To appear in *Proceedings of the International Conference on Advanced Monte Carlo for Radiation Physics, Particle Transport Simulation and Applications, Monte Carlo 2000* (P. Vas, Ed.), Lisbon, Portugal, 2000.

[8] A. Fassò, A. Ferrari, J. Ranft and P. R. Sala, FLUKA: Status and perspectives for hadronic applications. To appear in *Proceedings of the International Conference on Advanced Monte Carlo for Radiation Physics, Particle Transport Simulation and Applications, Monte Carlo 2000* (P. Vas, Ed.), Lisbon, Portugal, 2000.

[9] G. Battistoni, A. Ferrari, M. Carboni and V. Patera, Monte Carlo study of the arrival time distribution of particles in Extensive Air Showers in the energy range 1-100 TeV. *Astropart. Phys.* **9**, 277-295 (1998).

[10] G. Battistoni, A. Ferrari and E. Scapparone, Monte Carlo simulation of hadron production by atmospheric muons deep underground. *Nucl. Phys. B (Proc. Suppl.)* **70**, 480-482 (1999).

[11] W. Heinrich, S. Roesler and H. Schraube, Physics of cosmic radiation fields. *Radiat. Prot. Dosim.* **86**, 253-258 (1999).

[12] A. Ferrari, M. Pelliccioni and T. Rancati, The role of the quantities used in radiological protection for the assessment of the exposure to cosmic radiation. *Radiat. Prot. Dosim.* **83**, 199-210 (1999).

[13] G. Battistoni, A. Ferrari, P. Lipari, T. Montaruli, P. R. Sala and T. Rancati, A 3-dimensional calculation of atmospheric neutrino flux. *Astropart. Phys.* **12**, 315-333 (2000)

[14] A. Fassò and J. Poirier, Spatial and energy distribution of muons in γ-induced air showers. *Phys. Rev. D* **63**, 036002 (2001).

[15] J. Poirier, S. Roesler and A. Fassò, Distributions of secondary muons at sea level from cosmic gamma rays below 10 TeV. Preprint astro-ph / 0103030 (2001).

[16] A. Fassò, A. Ferrari, J. Ranft, P. R. Sala, G. R. Stevenson and J. M. Zazula, A comparison of FLUKA simulations with measurements of fluence and dose in calorimeter structures. *Nucl. Instrum. Methods A* **332**, 459-468 (1993).

[17] A. Ferrari and P. R. Sala, The physics of high energy reactions. In *Proceedings of the Workshop on Nuclear Reaction Data and Nuclear Reactors Physics, Design and Safety* (A. Gandini and G. Reffo, Eds.), p. 424. World Scientific, Singapore, 1998.

[18] A. Ferrari and P. R. Sala, Intermediate and high energy models in FLUKA: Improvements, benchmarks and applications. In *Proceedings of the International Conference on Nuclear Data for Science and Technology, NDST-97* (G. Reffo, A. Ventura and C. Grandi, Eds.), p. 247. Società Italiana di Fisica **59**, Part I, Bologna, 1997.

[19] V. Patera, M. Carboni, G. Battistoni and A. Ferrari, Simulation of the electromagnetic component of Extensive Air Showers. *Nucl. Instrum. Methods A* **356**, 514-525 (1995).

[20] A. Ferrari, T. Rancati and P. R. Sala, FLUKA applications in high energy problems: From LHC to ICARUS and atmospheric showers. In *Proceedings of The Third Workshop on Simulating Accelerator Radiation Environments (SARE-3)* (H. Hirayama, Ed.), p. 165. Proceedings 97-5, KEK, Tsukuba, Japan, 1997.

[21] A. Ferrari, J. Ranft and P. R. Sala, The FLUKA radiation transport code and its use for space problems. *Physica Medica* **XVII**, Suppl. 1, 72-80 (2000).

[22] E. Cuccoli, A. Ferrari and G. C. Panini, A group library from JEF 1.1 for flux calculations in the LHC machine detectors. ENEA-Bologna Report *JEF-DOC-340*, 1991.

[23] M. Boezio *et al.*, The cosmic-ray proton and helium spectra between 0.4 and 200 GV. *Astrophys. J.* **518**, 457-472 (1999).

[24] R. Bellotti *et al.*, Balloon measurements of cosmic ray muon spectra in the atmosphere along with those of primary protons and helium nuclei over midlatitude. *Phys. Rev. D* **60**, 052002 (1999).

[25] W. Menn *et al.*, The absolute flux of protons and helium at the top of the atmosphere using IMAX. *Astrophys. J.* **533**, 281-297 (2000).

[26] T. Sanuki *et al.*, Precise measurement of cosmic-ray proton and helium spectra with the BESS spectrometer. *Astrophys. J.* **545** 1135-1142 (2000).

[27] J. Alcaraz *et al.*, Cosmic protons. *Phys. Lett. B* **490**, 27-35 (2000).

[28] J. Alcaraz *et al.*, Helium in near Earth orbit. *Phys. Lett. B* **494**, 191-202 (2000).

[29] M. Ichimura *et al.*, Observation of heavy cosmic-ray primaries over the wide energy range from $\sim$ 100 GeV / particle to $\sim$ 100 TeV / particle: Is the celebrated "knee" actually so prominent? *Phys. Rev. D* **48**, 1949-1975 (1993).

[30] B. Wiebel, Chemical composition in high energy cosmic rays. Report *WU B 94-08*, 1994.

[31] M. J. Ryan, J. F. Ormes and V. K. Balasubrahmanyan, Cosmic-ray proton and helium spectra above 50 GeV. *Phys. Rev. Lett.* **28**, 985 (1972).

[32] K. Asakimori *et al.*, Cosmic-ray proton and helium spectra: Results from the JACEE experiment. *Astrophys. J.* **502**, 278-283 (1998).

[33] G. D. Badhwar, The radiation environment in low-Earth orbit. *Radiat. Res.* **148**, S3-S10 (1997).

[34] G. D. Badhwar, P. M. O'Neill and A. G. Troung, Galactic cosmic radiation environmental models. Unpublished, 2000.

[35] University of Chicago, `http://ulysses.uchicago.edu/NeutronMonitor/`.

[36] D. F. Smart and M. A. Shea, World grid of cosmic ray vertical cutoff rigidities for Epoch 1990.0, In *Proceedings of 25th International Cosmic Ray Conference*, pp. 401-404, Durban, South Africa, 1997.

[37] D. F. Smart and M. A. Shea, private communication, 2000.

[38] G. D. Badhwar, private communication, 1998

[39] I. Lux and L. Koblinger, *Monte Carlo Particle Transport Methods: Neutron and Photon Calculations*. CRC Press, Boca Raton, 1991.

[40] H. Schraube, J. Jakes, A. V. Sannikov, E. Weitzenegger, S. Roesler and W. Heinrich, The cosmic ray induced neutron spectrum at the summit of the Zugspitze (2963 m). *Radiat. Prot. Dosim.* **70**, 405-408 (1997).

[41] W. N. McElroy, S. Berg, T. Crockett and R. G. Hawkins, Spectra unfolding. Report *AFWL-TR-67-41 1-4*, 1967.

[42] P. Goldhagen, M. Reginatto, J. W. Wilson, R. C. Singleterry, I. W. Jones and T. Kniss, Measurement of the energy spectrum of cosmic-ray induced neutrons aboard a high-altitude airplane and on the ground. In *Transactions of the American Nuclear Society 2000 Winter Meeting*, Vol. **83**, pp. 261-262, 2000.

[43] P. Goldhagen, M. Reginatto, T. Kniss, J. W. Wilson, R. C. Singleterry, I. W. Jones and W. Van Steveninck, Measurement of the energy spectrum of cosmic-ray induced neutrons aboard an ER-2 high-altitude airplane. In *Proceedings of the International Workshop on Neutron Field Spectrometry in Science, Technology and Radiation Protection*, Pisa, Italy, June 4-8, 2000, *Nucl. Instrum. Methods A* in press (2001).

[44] H. Schraube *et al.*, in preparation.

[45] D. L. Randel *et al.*, A new global water vapor dataset. *Bulletin of the American Meteorological Society* **77**, 1233-1246 (1996).

[46] P. Goldhagen, Overview of aircraft radiation exposure and recent ER-2 measurements. *Health Physics* **79**, 526-544 (2000).

[47] M. Reginatto and P. Goldhagen, MAXED, A computer code for the deconvolution of multisphere neutron spectrometer data using the Maximum Entropy Method. Environmental Measurements Laboratory Report *EML-595*, 1998.

[48] P. Goldhagen, private communication, 2001.

[49] H. Kornmayer, H. H. Mielke, J. Engler and J. Knapp, High-energy cosmic ray neutrons at sea level. *J. Phys. G, Nucl. Part. Phys.* **20**, 439-449 (1995).

[50] N. M. Kocharian *et al.*, Energy spectra and nuclear interactions of cosmic-ray particles. *Sov. Phys. JETP*, **35**, 933-942 (1959).

[51] M. Boezio *et al.*, Measurement of the flux of atmospheric muons with the CAPRICE94 apparatus. *Phys. Rev. D* **62**, 032007 (2000).

[52] J. Kremer *et al.*, Measurements of ground-level muons at two geomagnetic locations. *Phys. Rev. Lett.* **83**, 4241-4244 (1999).

[53] R. Beaujean, J. Kopp and G. Reitz, Radiation exposure in civil aircraft. *Radiat. Prot. Dosim.* **85**, 287-290 (1999).

[54] J. Kopp, Kiel University, private communication, 2000.

[55] M. Boezio *et al.*, Atmospheric electron flux at airplane altitude. *Phys. Rev. D* **44**, 3419-3426 (1991).

[56] M. Pelliccioni, Overview of fluence-to-effective dose and fluence-to-ambient dose equivalent conversion coefficients for high energy radiation calculated using the FLUKA code. *Radiat. Prot. Dosim.* **88**, 279-297 (2000).

[57] International Commission on Radiological Protection, *1990 Recommendations of the International Commission on Radiological Protection*. ICRP Publication 60, Pergamon Press, Oxford, 1991.

[58] U. J. Schrewe, Global measurement of the radiation exposure of civil air crew from 1997 to 1999. *Radiat. Prot. Dosim.* **91**, 347-364 (2000).

[59] U. J. Schrewe, private communication, 2000.

[60] B. J. Lewis *et al.*, Aircrew exposure from cosmic radiation on commercial airline routes. *Radiat. Prot. Dosim.* **93**, 293-314 (2001).

[61] B. J. Lewis, private communication, 2000.

[62] V. Mares, A. V. Sannikov and H. Schraube, Response functions of the Andersson-Braun and extended range REM counters for neutron energies from thermal to 10 GeV. In *Proceedings of the International Workshop on Neutron Field Spectrometry in Science, Technology and Radiation Protection*, Pisa, Italy, June 4-8, 2000, *Nucl. Instrum. Methods A* in press (2001).

[63] P. A. Chee, L. A. Braby and T. J. Conroy, Potential doses to passengers and crew of supersonic transports. *Health Physics* **79**, 547-552 (2000).

[64] B. Ellaschuk, private communication, 2001.

Table 1: Summary of date and location of the low-energy proton and helium spectra measurements. The solar modulation parameter (3rd column) was determined from the Climax count rate according to the model of Badhwar [33]. The average vertical rigidity cutoff, $R_{\rm v}$, for the measurement locations was obtained from the tabulation by Smart and Shea [36].

Experiment	Date	Sol. Mod. (MV)	Latitude	Longitude	$R_{\rm v}$ (GV)
AMS [27, 28]	98-06	471	-	-	-
BESS [26]	98-07-(29-30)	642	56.5° N	101.0° W	0.41
CAPRICE [23]	94-08-(08-09)	698	56.15°-56.5° N	101.0°-117.2° W	0.41
IMAX [25]	92-07-16	902	56.5° N	101.0° W	0.41
MASS [24]	91-09-23	1529	34.43°-35.29° N	103.38°-104.25° W	4.06

Table 2: Summary of the environmental conditions considered in the five calculations for the experiment at the Schneefernerhaus. The geometry in the first calculation consisted of air down to sea level. In the other calculations the geometry was truncated by a concrete floor at the altitude of the Schneefernerhaus.

Calculation No.	Water Vapor (7.5 mm)	Al-Container (2×2 mm)	Snow (10 cm)	Concrete Floor (10 cm)
1	-	-	-	-
2	yes	-	-	yes
3	-	yes	-	yes
4	yes	yes	yes	yes
5	yes	yes	-	yes

Table 3: Comparison of experimental and calculated Bonner sphere neutron count rates for the measurement at the Schneefernerhaus. Detector 1 is an unshielded ^{3}He counter; the other detectors are surrounded by polyethylene spheres of different diameters. Detector 12 has a lead converter embedded in 9 inches of polyethylene and is therefore sensitive to high energy neutrons. The calculated count rates are shown for five different environmental conditions (see Table 2) and were obtained by folding neutron spectra with the Bonner sphere response functions. All count rates are in units of s^{-1}.

Det. No.	Diameter (inch)	Exp.	FLUKA (1)	(2)	(3)	(4)	(5)
1	0	0.0289	0.0571	0.0496	0.0505	0.0533	0.0501
2	2.5	0.0418	0.1099	0.1008	0.1062	0.0702	0.1030
3	3.0	0.0575	0.1569	0.1425	0.1511	0.0941	0.1460
4	4.0	0.0803	0.2249	0.2018	0.2154	0.1290	0.2077
5	5.0	0.0888	0.2484	0.2232	0.2388	0.1436	0.2303
6	6.0	0.0871	0.2409	0.2184	0.2335	0.1436	0.2257
7	7.0	0.0850	0.2157	0.1978	0.2110	0.1337	0.2045
8	9.0	0.0707	0.1552	0.1465	0.1550	0.1058	0.1512
9	10.0	0.0623	0.1313	0.1256	0.1323	0.0938	0.1295
10	12.0	0.0478	0.0933	0.0913	0.0952	0.0725	0.0937
11	15.0	0.0345	0.0629	0.0627	0.0645	0.0537	0.0638
12	9.2	0.1871	0.3514	0.3357	0.3481	0.2754	0.3414

Table 4: Summary of the measurement conditions of Refs. [42, 43]. The solar modulation parameter was determined from the Climax count rate at the respective dates according to the model of Badhwar [33]. The average vertical rigidity cutoff, R_{v}, for the measurement locations was obtained from the tabulation by Smart and Shea [36].

Measurement No.	Date	Latitude / Longitude	Altitude (km)	Sol. Mod. (MV)	R_{v} (GV)	Depth ($\mathrm{g/cm^2}$)
1	97-06-11	19° N / 127° W	20.3	480.4	11.9	53
2	97-06-13	54° N / 117° W	20.0	481.1	0.8	56
3	97-06-13	56° N / 121° W	16.2	481.1	0.7	101
4	97-06-(08-15)	38° N / 122° W	11.9	480.0	4.3	201

Table 5: Comparison of experimental and calculated neutron count rates for different Bonner sphere detectors and the four measurements performed aboard of the ER-2 airplane [42, 43] (see Table 4). Detector 1 is an unshielded ^{3}He counter, detector 2 is surrounded by a cadmium layer and the other detectors are surrounded by polyethylene spheres of different diameters. The sphere diameters are listed in the second column and were taken from Ref. [43]. Detectors 13 and 14 have the same polyethylene thickness as detectors 11 and 12, respectively, but, additionally, they have lead and steel shells embedded. Detectors 3 and 5 were not flown. The calculated count rates were obtained by folding neutron spectra with the Bonner sphere response functions [43, 48]. All count rates are in units of s^{-1}.

Det.	Diameter	Meas. No. 1		Meas. No. 2		Meas. No. 3		Meas. No. 4	
No.	(inch)	Exp.	FLUKA	Exp.	FLUKA	Exp.	FLUKA	Exp.	FLUKA
1	-	0.84	0.66	6.76	5.26	7.08	5.56	2.45	1.96
2	-	0.40	0.34	3.19	2.74	3.20	2.87	1.11	1.01
4	3.234	2.67	2.67	21.42	21.26	22.11	21.82	7.76	7.59
6	4.626	5.29	5.30	42.06	42.19	42.29	42.41	15.00	14.66
7	5.626	5.86	5.98	47.17	47.62	46.11	47.41	16.16	16.34
8	6.814	5.57	5.73	44.65	45.66	43.41	44.96	15.12	15.44
9	8.232	4.99	4.80	39.51	38.14	36.63	37.08	12.82	12.70
10	9.830	4.03	3.69	30.41	29.31	28.06	28.16	10.07	9.63
11	11.846	2.53	2.59	20.02	20.63	18.30	19.63	6.67	6.70
12	14.974	1.66	1.71	12.44	13.63	11.48	12.82	4.12	4.38
13	11.848	7.07	7.92	45.82	52.43	41.58	48.28	15.99	16.51
14	15.030	2.57	3.18	18.22	22.41	16.57	20.66	6.23	7.07

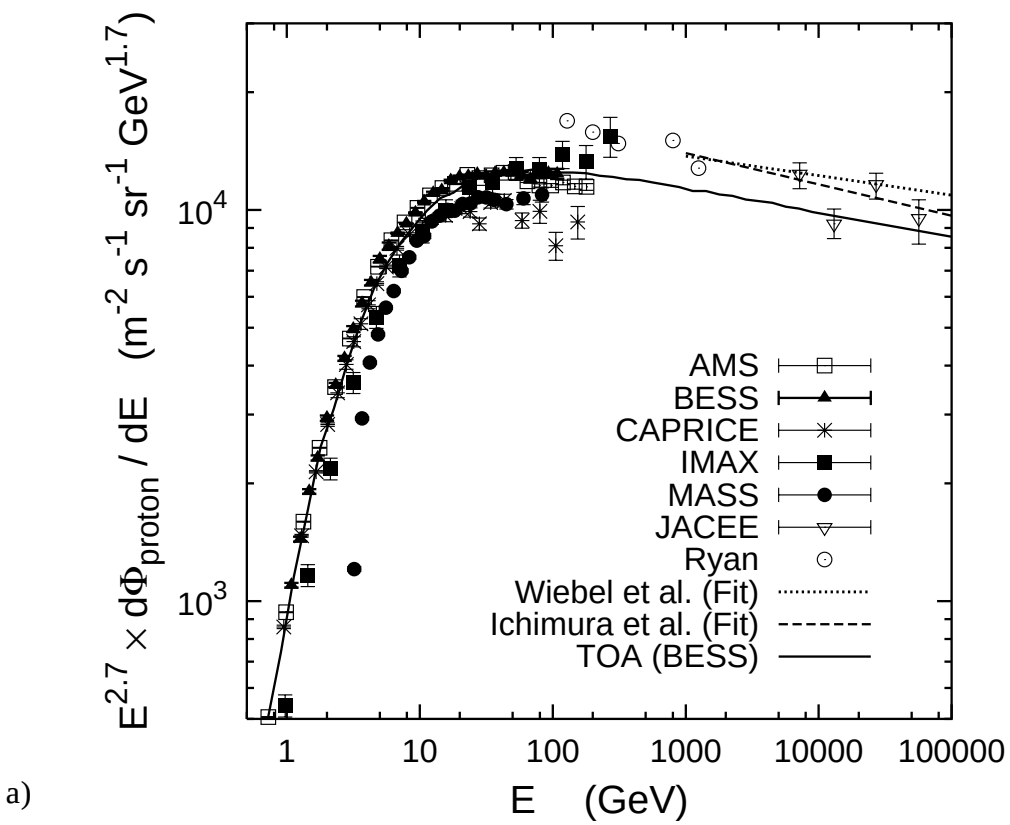

a)

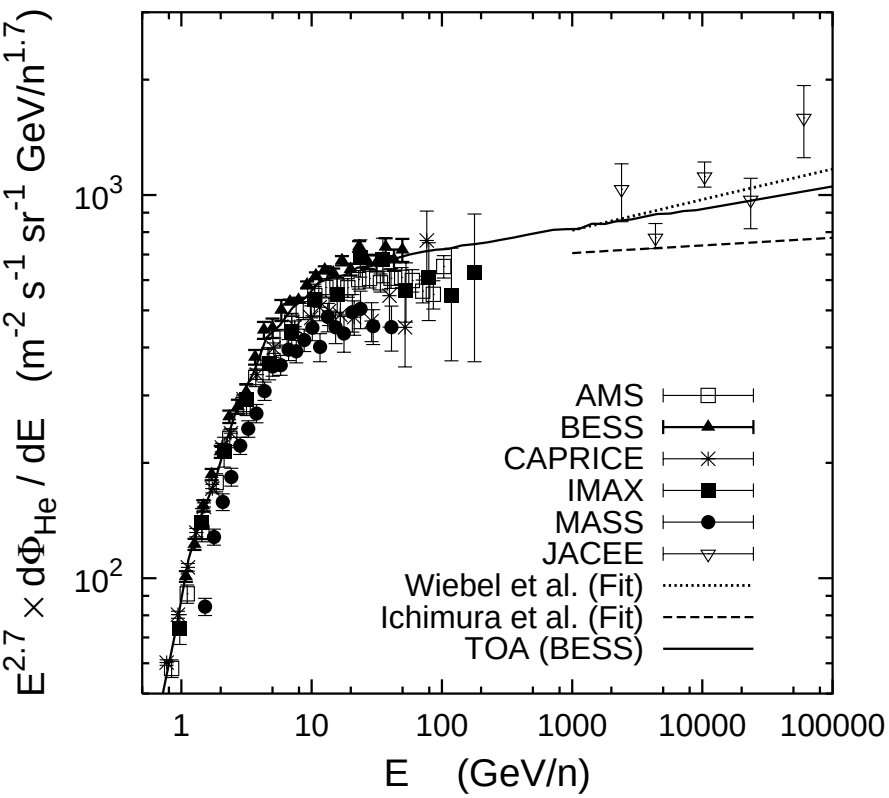

b)

Figure 1: Summary of direct measurements of the cosmic ray proton (a) and helium spectrum (b) on top of the atmosphere (symbols) [23, 24, 25, 26, 27, 28, 31, 32]. Dashed and dotted lines represent two fits to data at higher energies [29, 30]. In addition, the spectrum used in this work and as modulated for the conditions of the BESS experiment is shown (labelled "TOA (BESS)"). All spectra are multiplied by $E^{2.7}$ in order to emphasize the high-energy part.

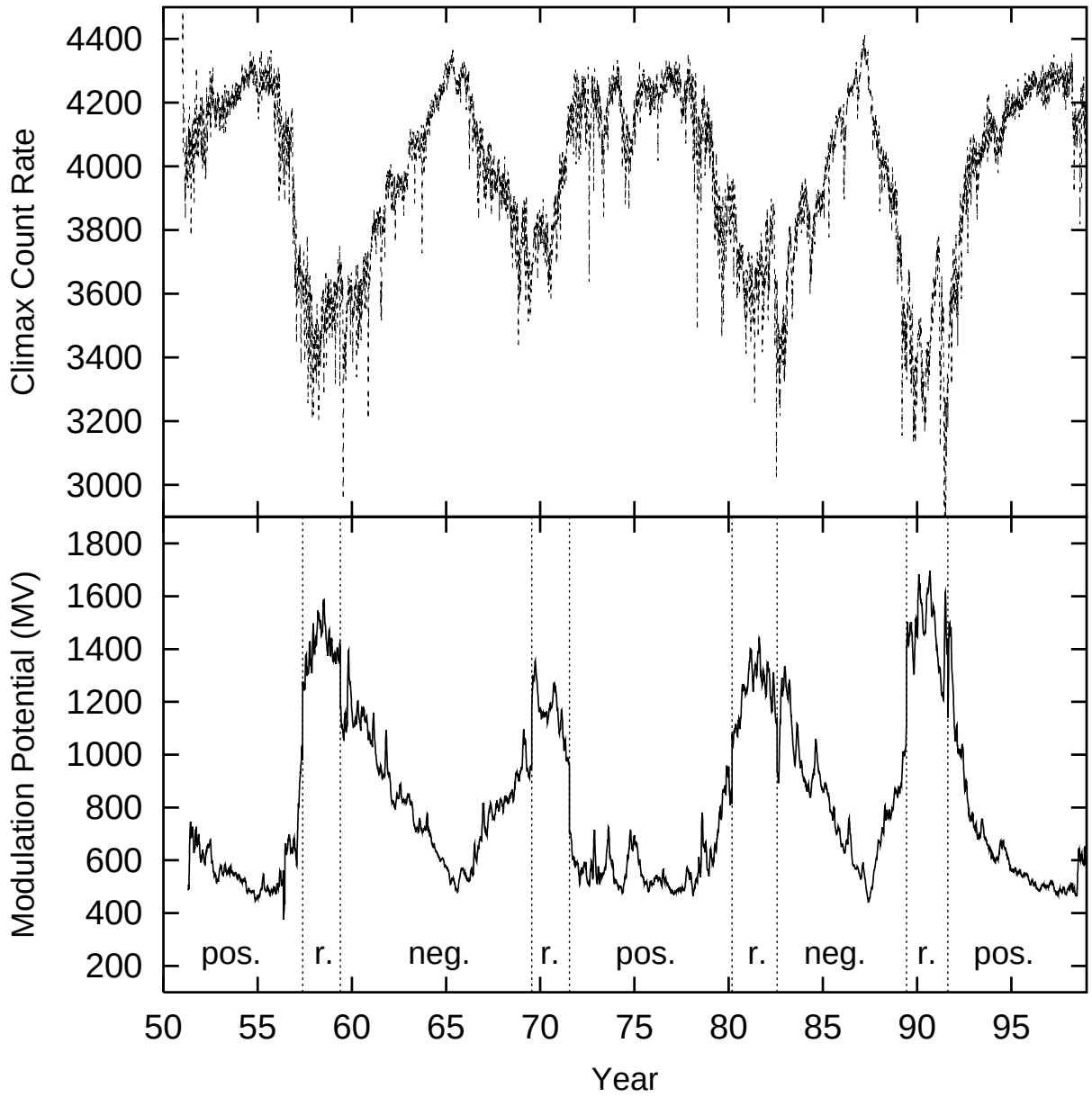

Figure 2: Solar modulation for the period of time between 1950 and 2000. The upper graph shows the daily Climax neutron monitor count rate [35]. The corresponding modulation potentials are given in the lower graph. Vertical dotted lines indicate periods of positive and negative field polarity and of field reversal (labelled "r.").

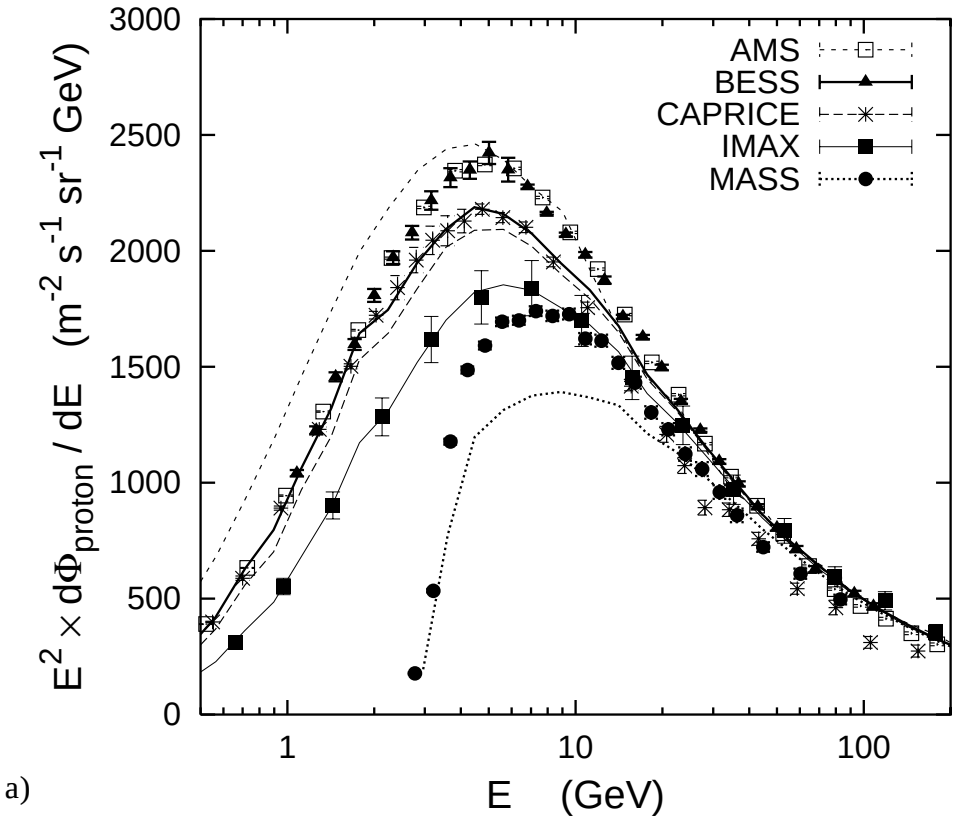

a)

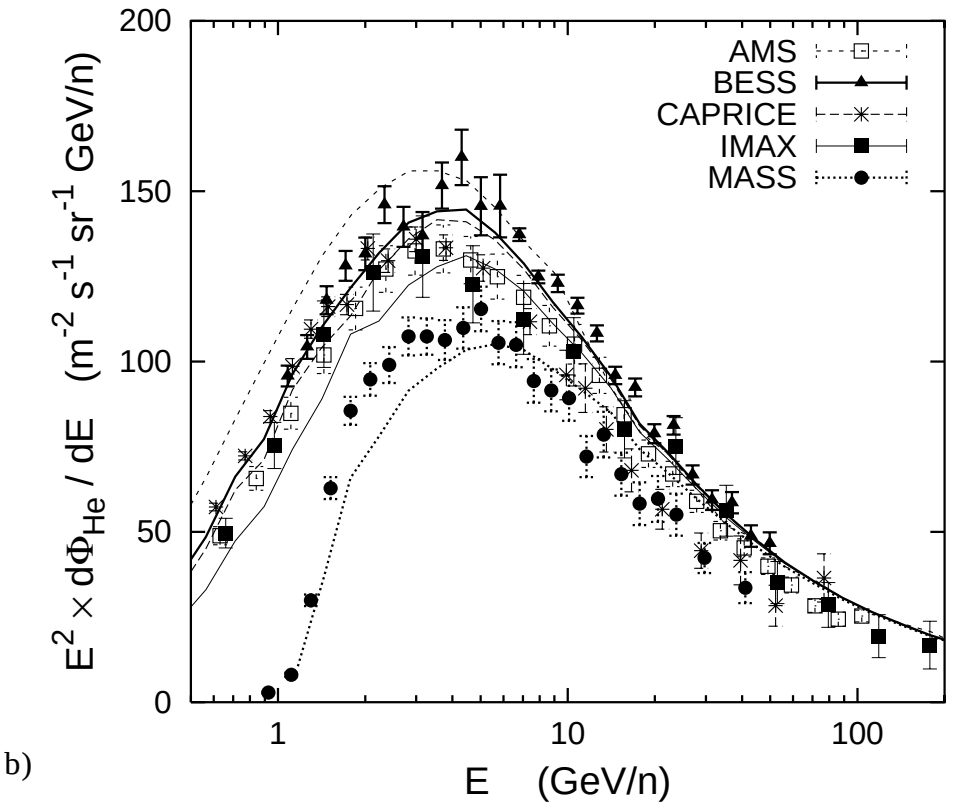

b)

Figure 3: Summary of measured proton (a) and helium spectra (b). Data as in Fig. 1 (symbols). Here, all spectra are multiplied by E^2 in order to emphasize the medium and low-energy part. The spectra used in this work and as modulated for the five measurement conditions are shown as curves.

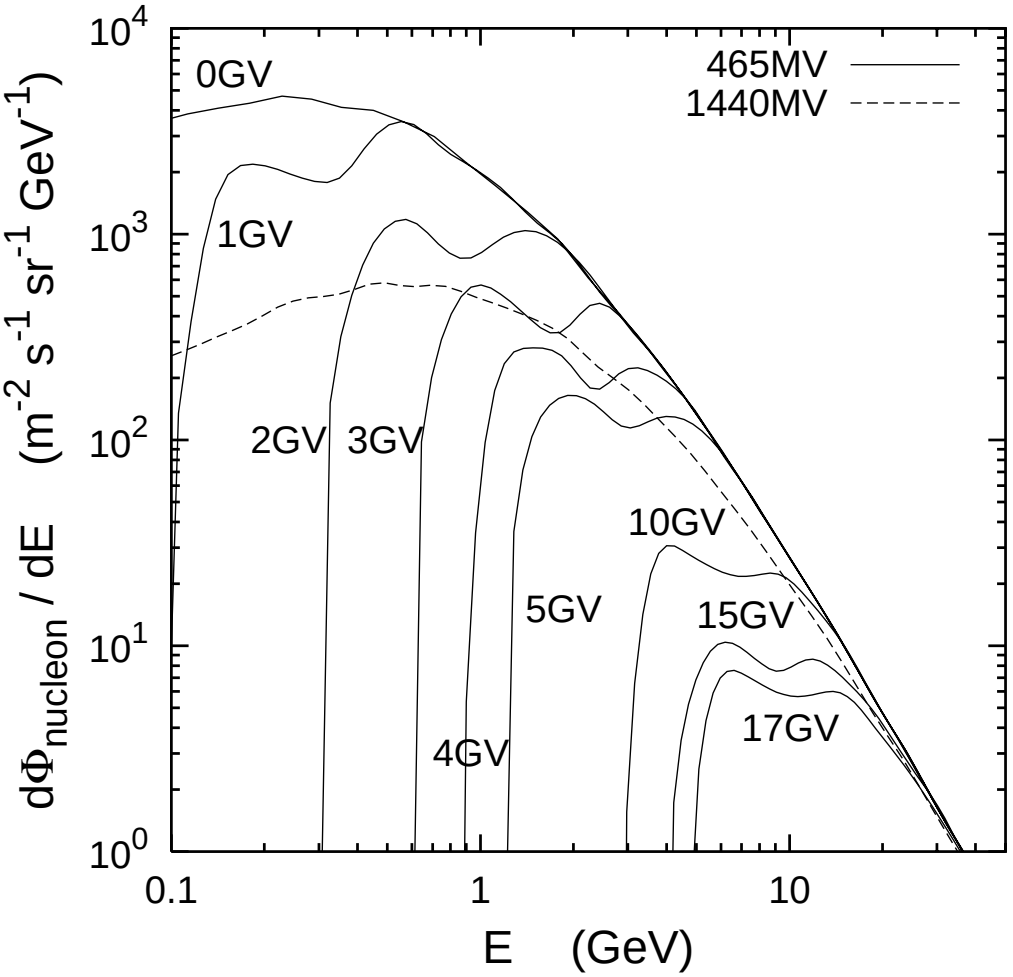

Figure 4: Total nucleon flux for solar minimum modulation (465 MV) and different vertical rigidity cutoffs. In addition, the flux at solar maximum modulation (1440 MV) is shown.

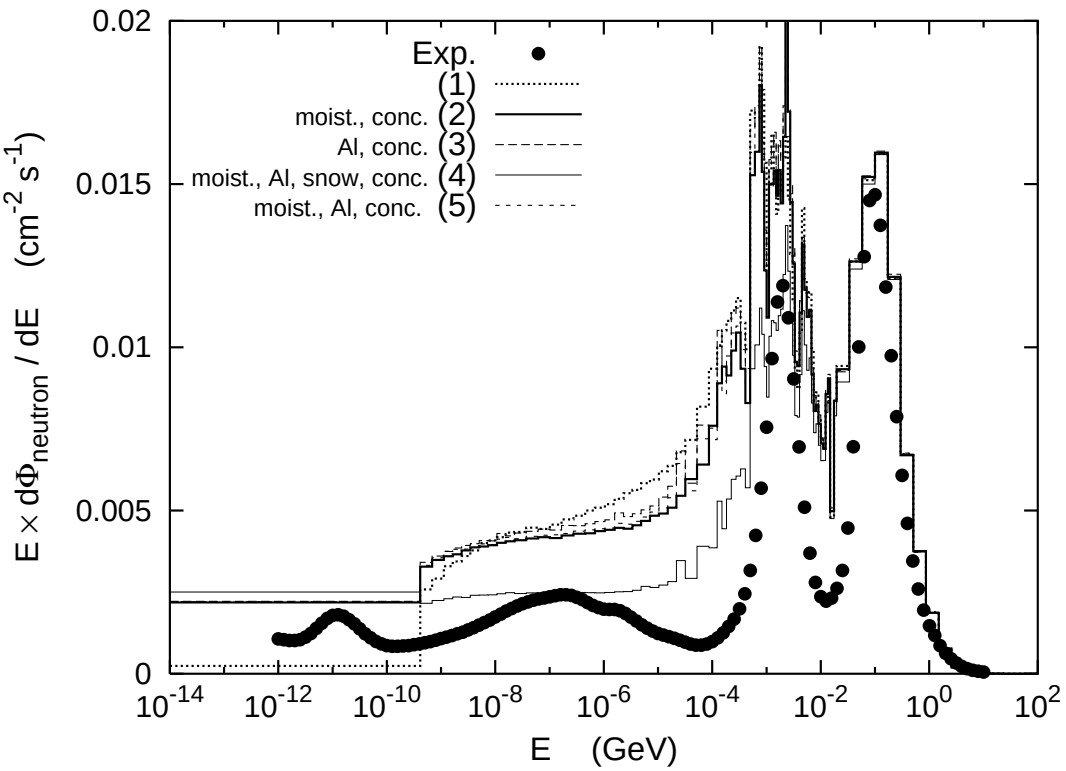

Figure 5: Measured (symbols drawn at the geometric average of lower and upper bin edges) and calculated (histograms) ground-level neutron spectra for the experiment at the Schneefernerhaus. The calculations were performed for five different environmental conditions which are summarized in Table 2.

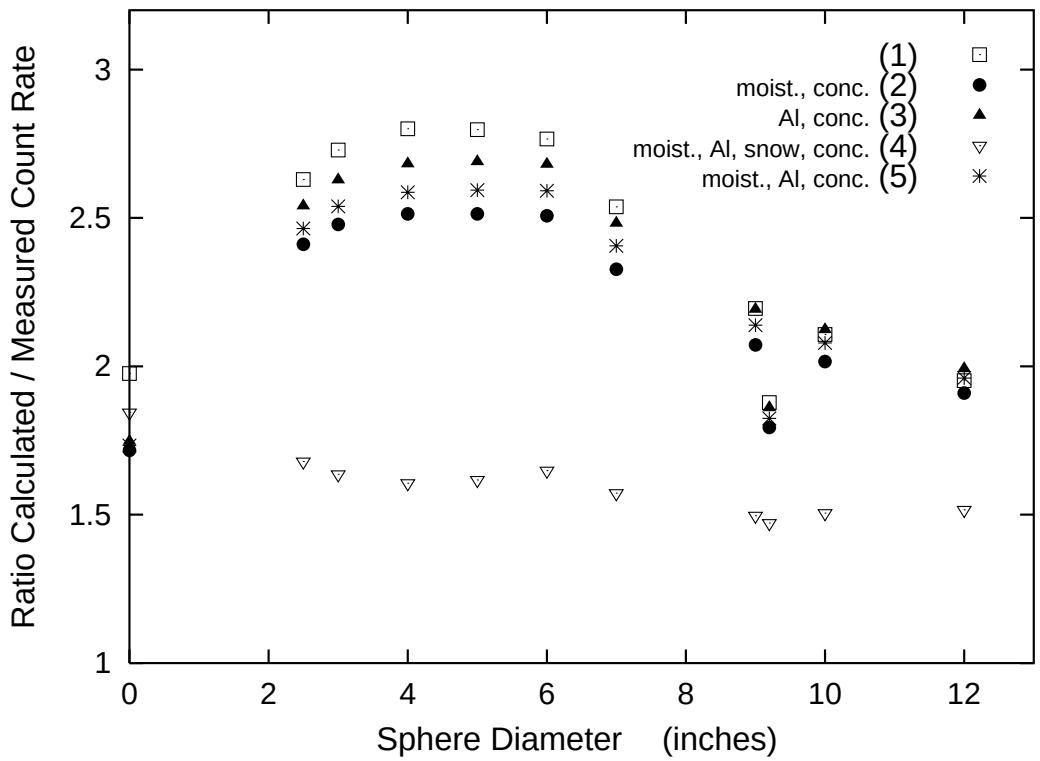

Figure 6: Ratio of calculated and measured Bonner sphere count rates as given in Table 3 for the experiment at the Schneefernerhaus. The detector of a diameter of 9.2 inches has a lead converter embedded in a 9 inch polyethylene sphere and is therefore sensitive to high energy neutrons. The environmental conditions assumed in the five calculations are summarized in Table 2.

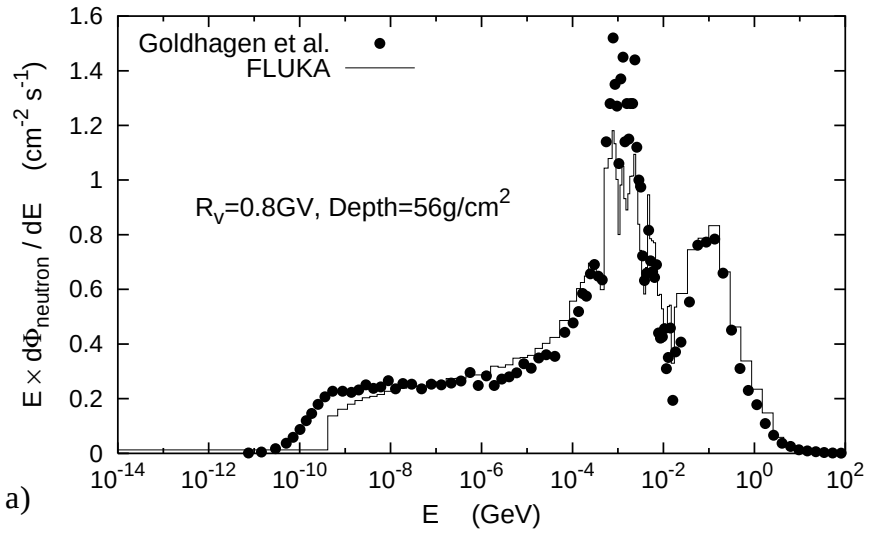

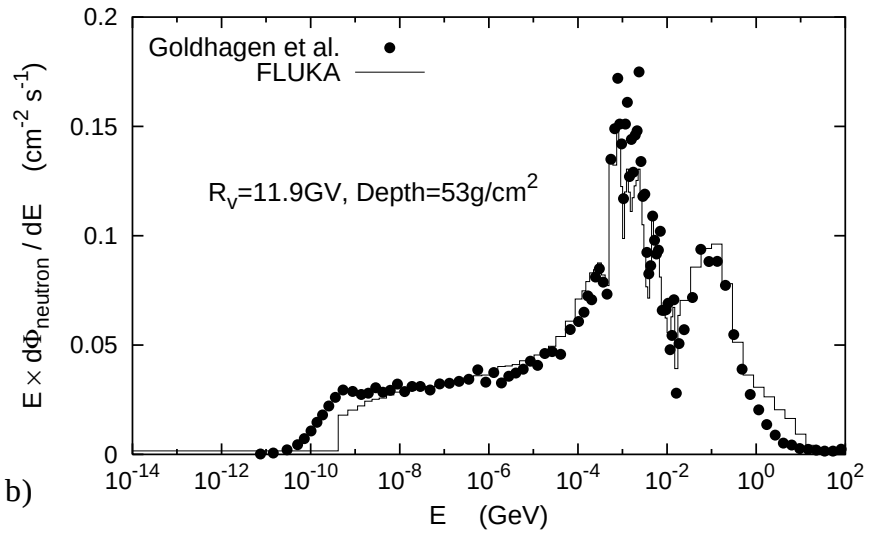

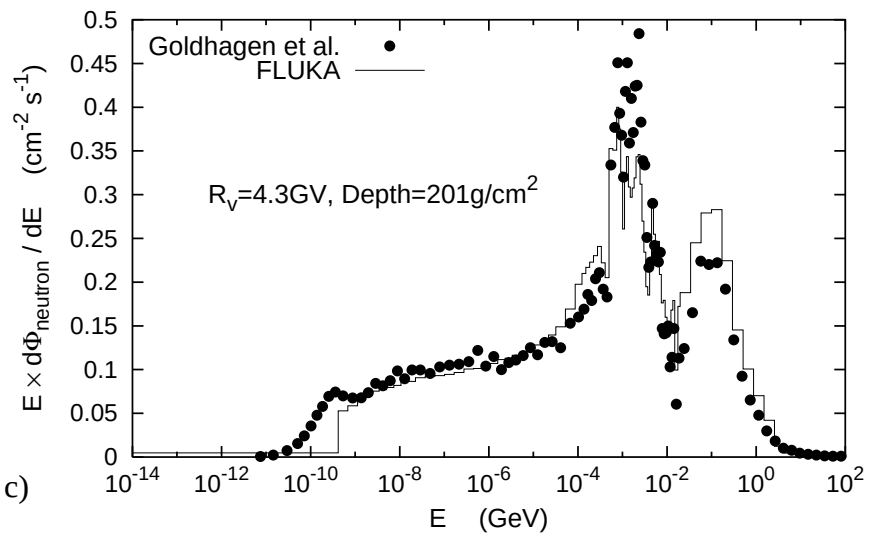

Figure 7: Atmospheric neutron spectra measured aboard of an ER-2 high-altitude airplane [42, 43] (symbols) and calculated with FLUKA (histograms). The three graphs show results for different geographic locations and altitudes. Graphs a), b), and c) correspond to measurement conditions 2, 1, and 4, respectively, of Table 4.

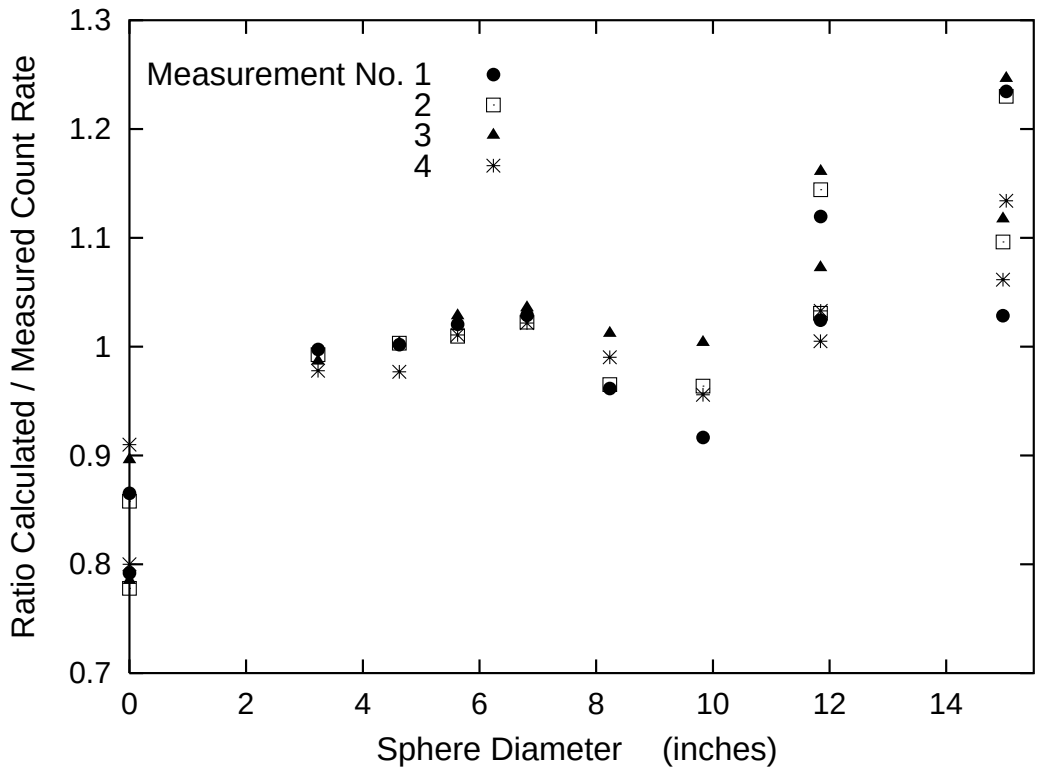

Figure 8: Ratio of calculated and measured count rates as given in Table 5 for the different Bonner sphere detectors flown on the ER-2 airplane. The conditions of the four measurements are summarized in Table 4. At about 12 and 15 inches diameter there are two data points for each measurement condition. The higher of the two values are for the lead- and steel-modified spheres which are sensitive to high-energy neutrons.

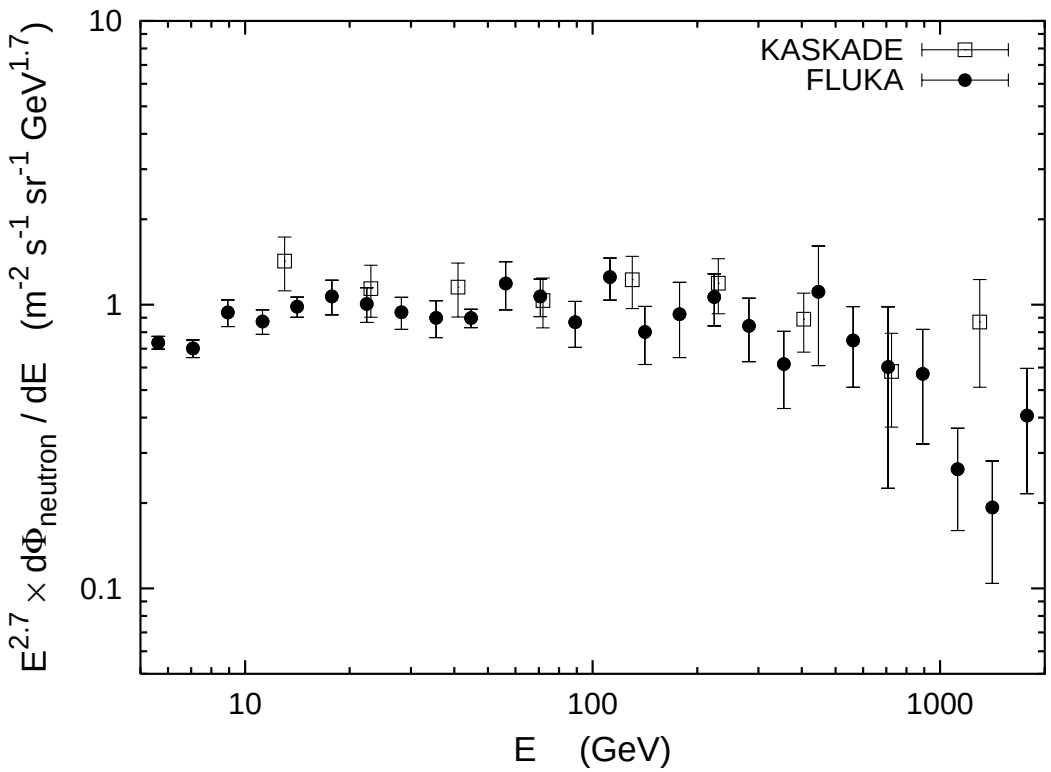

Figure 9: Vertical neutron flux at sea level. Data of the KASKADE experiment [49] are compared to FLUKA results. The spectra are multiplied by $E^{2.7}$ which corresponds to the inverse of the energy behavior of the flux at high energy.

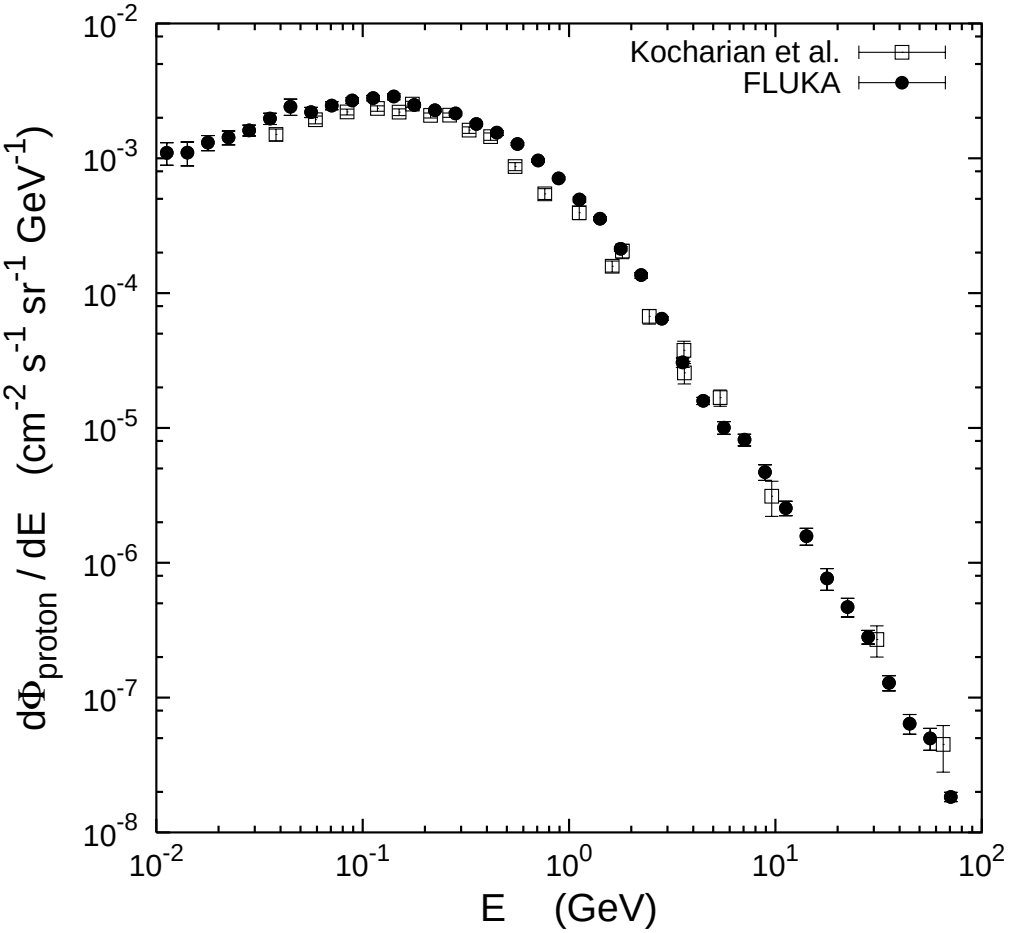

Figure 10: The vertical proton flux measured at 3200 m above sea level [50] is compared to FLUKA results.

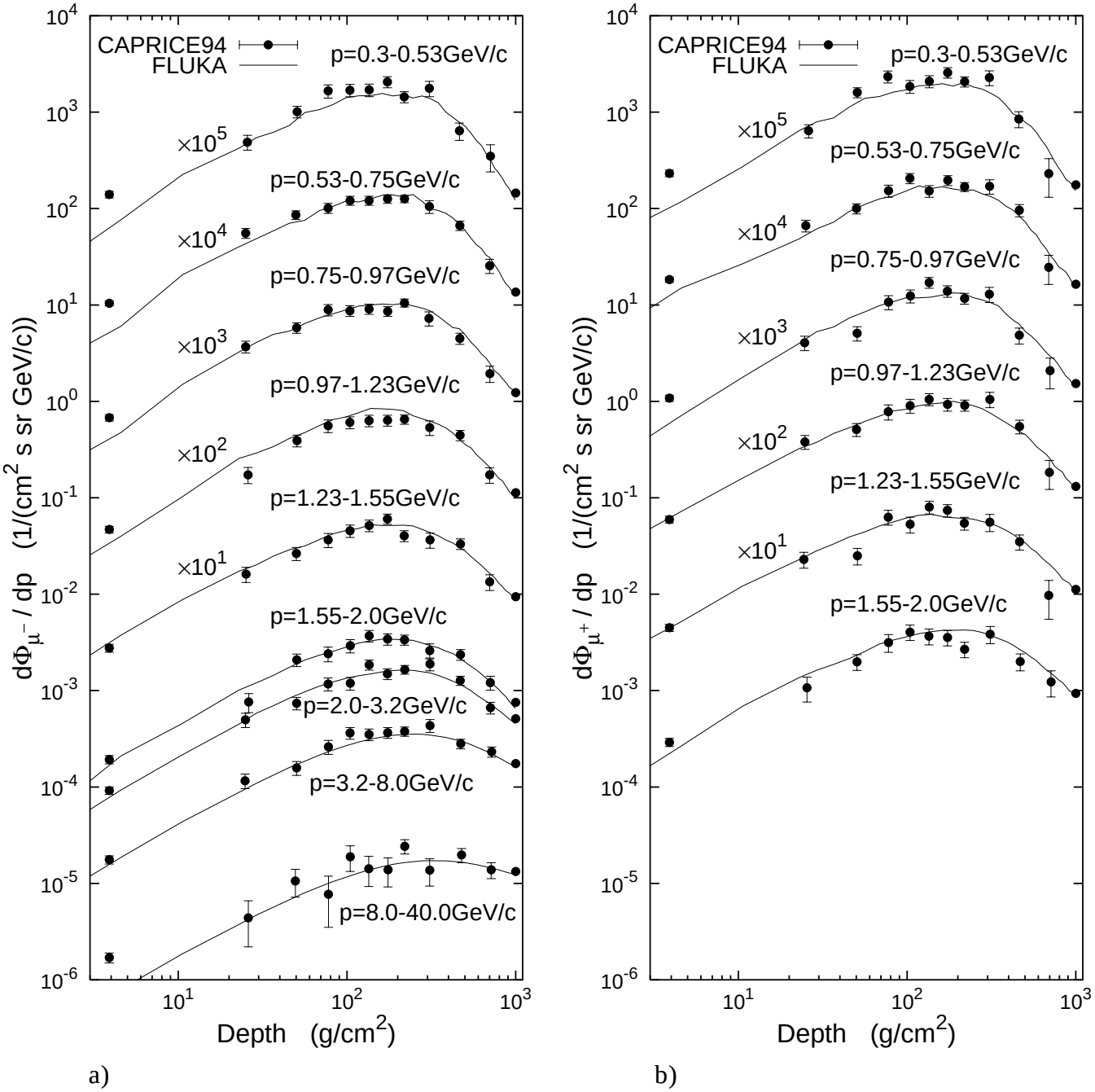

Figure 11: Dependence of the negative (a) and positive muon flux (b) on the depth in the atmosphere shown for different intervals of the muon momentum. FLUKA results (curves) are compared to data obtained by the CAPRICE experiment [51] (symbols). Fluxes for the five lowest momentum intervals were shifted by constant factors as indicated.

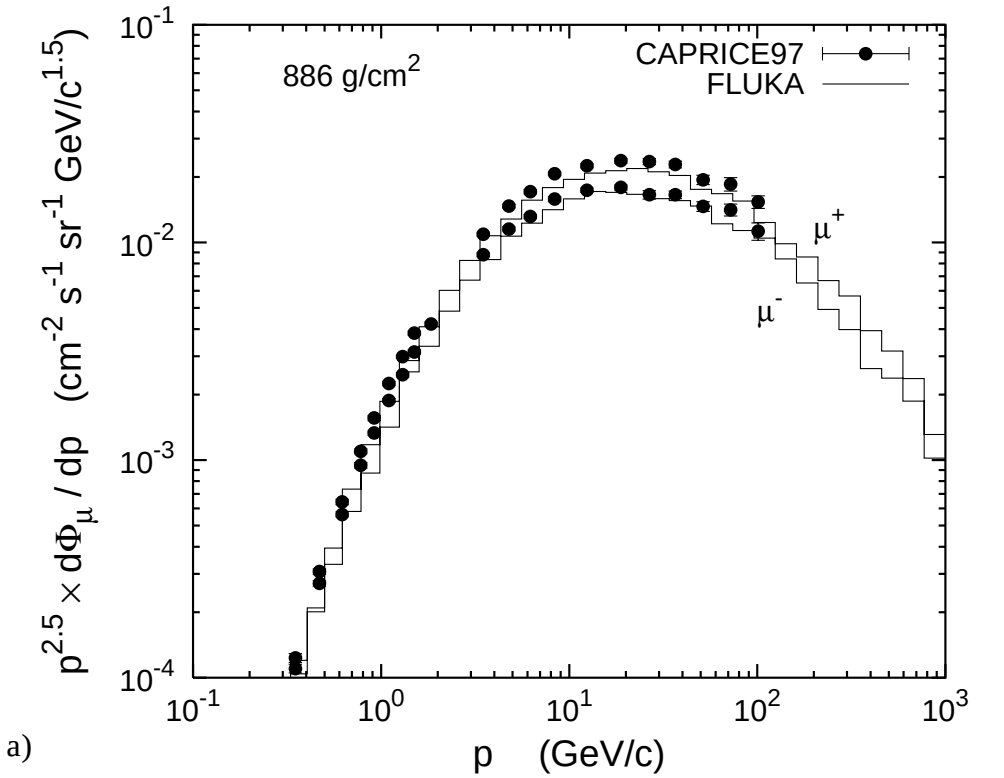

a)

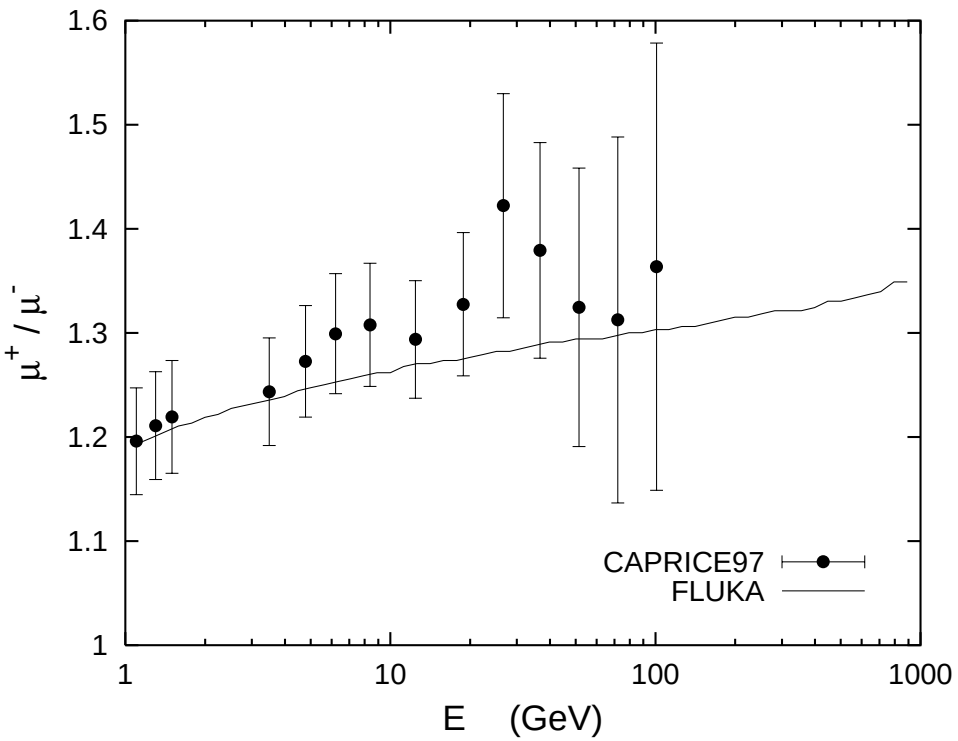

b)

Figure 12: a) Energy spectra of positive and negative muons as measured at a depth of 886 g/cm^2 by the CAPRICE experiment [52] (symbols) are compared to FLUKA results (histograms). The spectra are shown as function of the muon momentum. b) Ratio of the yields of positive and negative muons as a function of the kinetic energy of the muon. Experimental data by CAPRICE [52] (symbols) are compared to FLUKA results (curve).

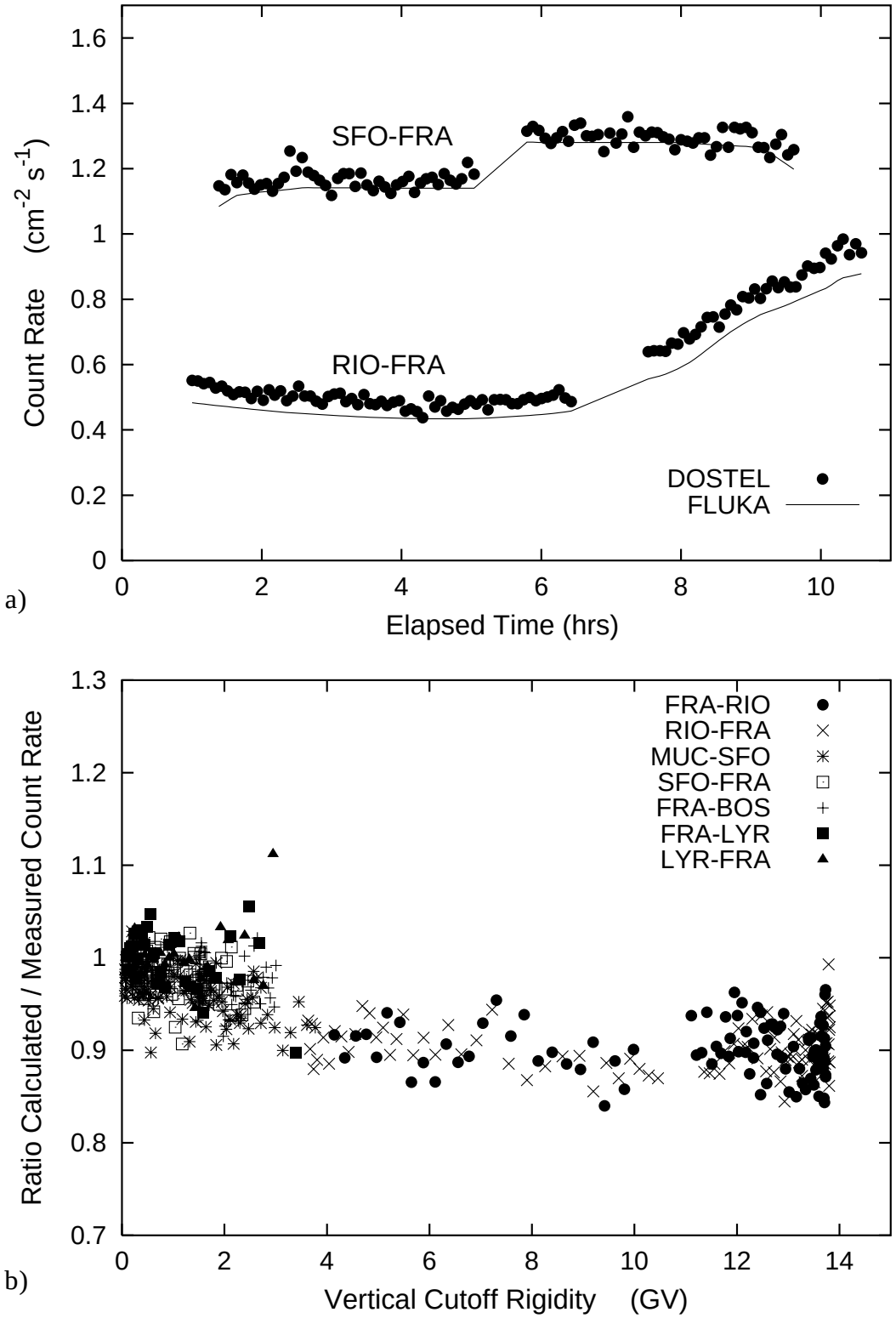

Figure 13: Comparison of FLUKA results and measurements of ionizing radiation for various commercial flights from / to Boston (BOS), Frankfurt (FRA), Longyearbyen (LYR), Munich (MUC), Rio de Janeiro (RIO), and San Francisco (SFO). a) DOSTEL count rates and the calculated current of charged particles are shown as function of the elapsed time after take-off for two selected flights (San Francisco - Frankfurt and Rio de Janeiro - Frankfurt). b) The ratio of calculated and measured count rates is shown for all flights as function of the vertical rigidity cutoff.

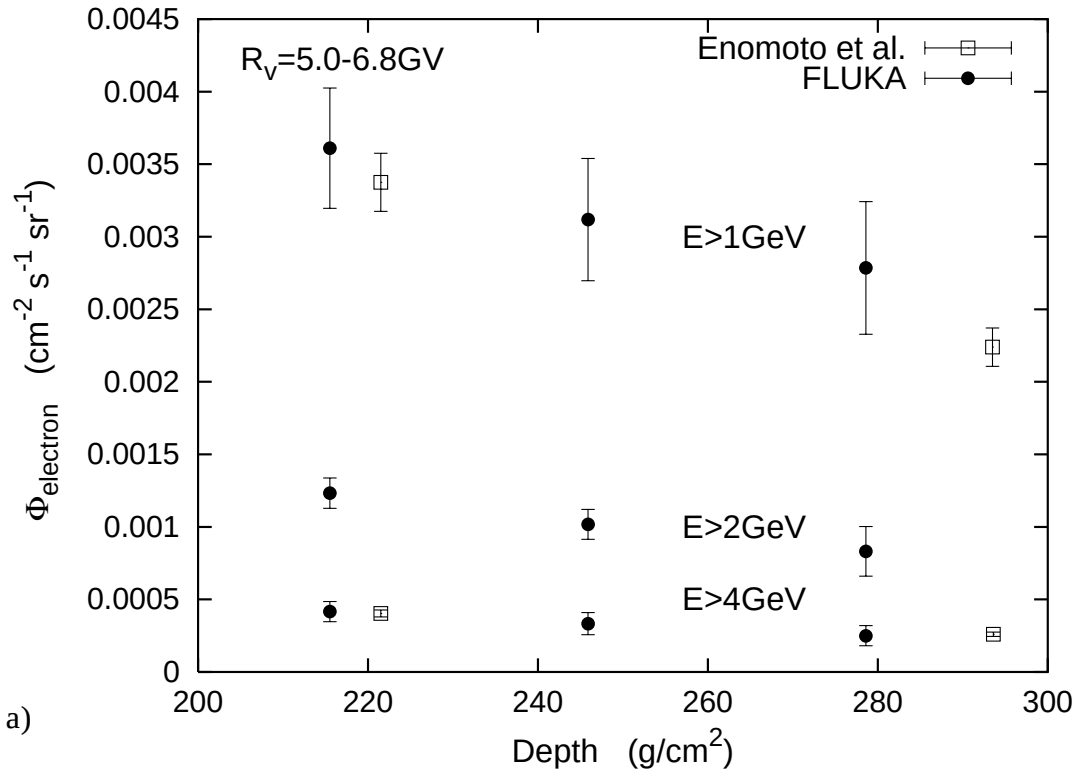

a)

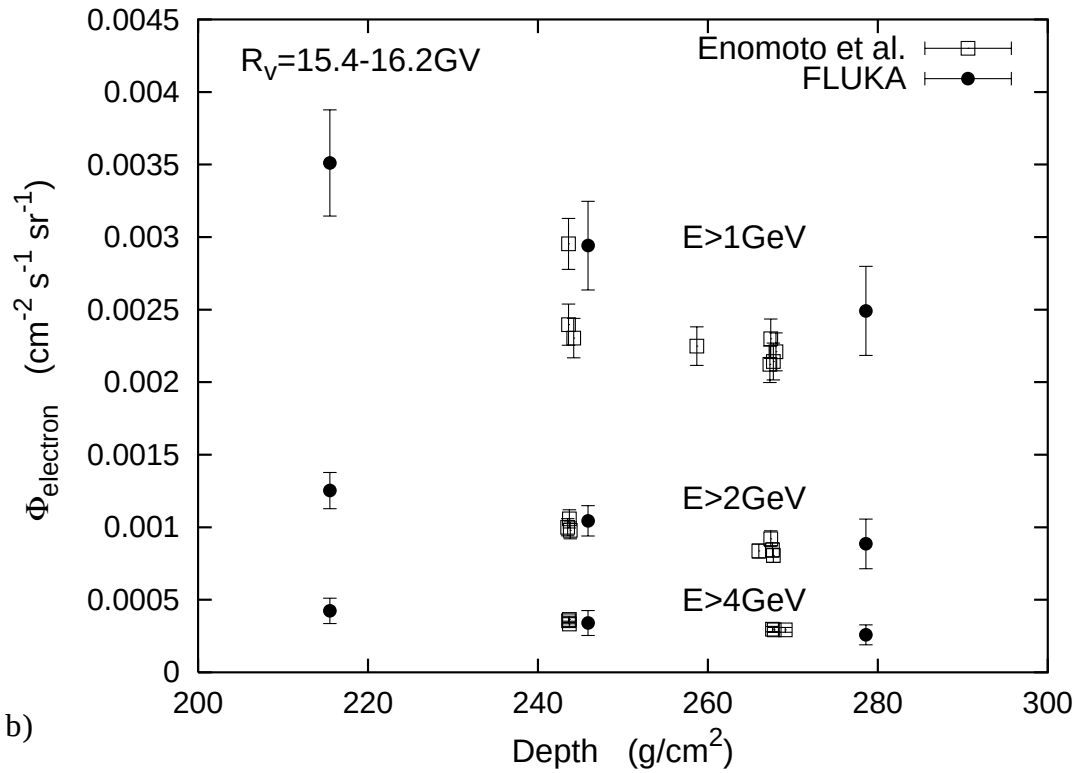

b)

Figure 14: Vertical electron flux as function of atmospheric depth for typical aircraft altitudes. a) Results of FLUKA calculations for a vertical rigidity cutoff $R_v = 5.9$ GV are compared to experimental data [55] obtained for cutoffs between 5.0 GV and 6.8 GV. Similarly, in b) FLUKA results for $R_v = 15.9$ GV are compared to data for cutoffs between 15.4 GV and 16.2 GV.

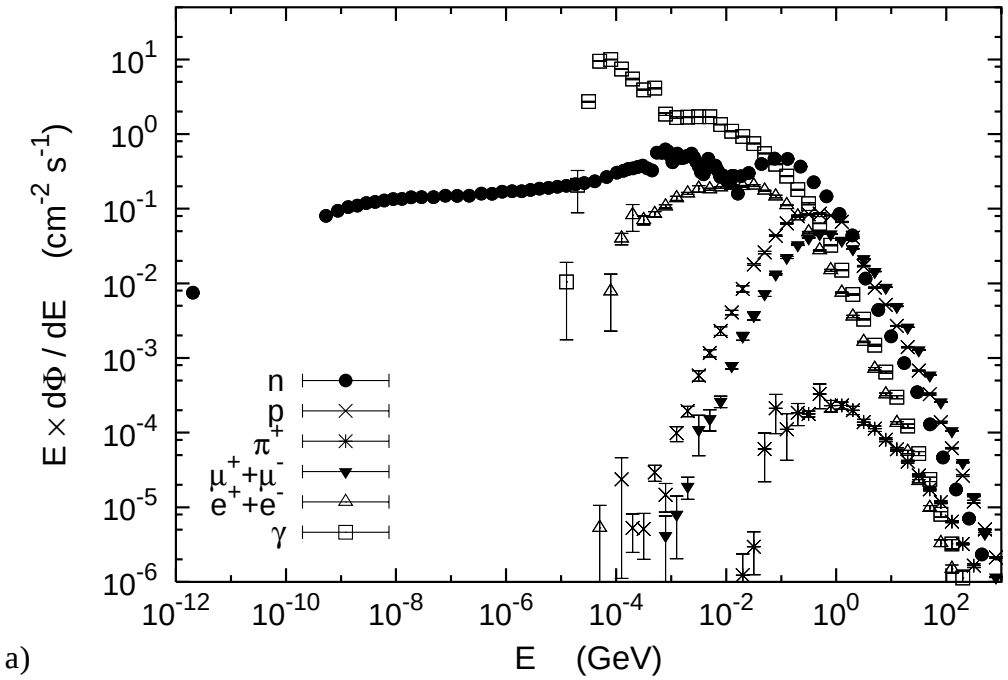

a)

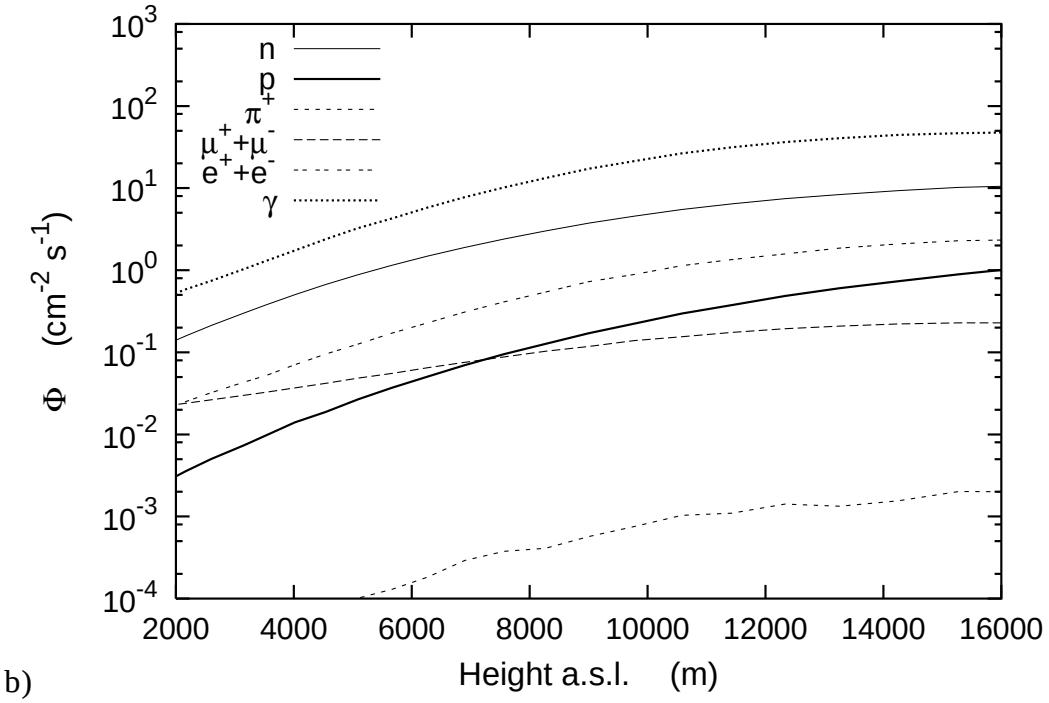

b)

Figure 15: a) Energy spectra of different particles for solar minimum (465 MV), geomagnetic pole (R_v=0), and a height above sea level of 10580 m. b) Energy-integrated particle fluence rate as function of the height above sea level.

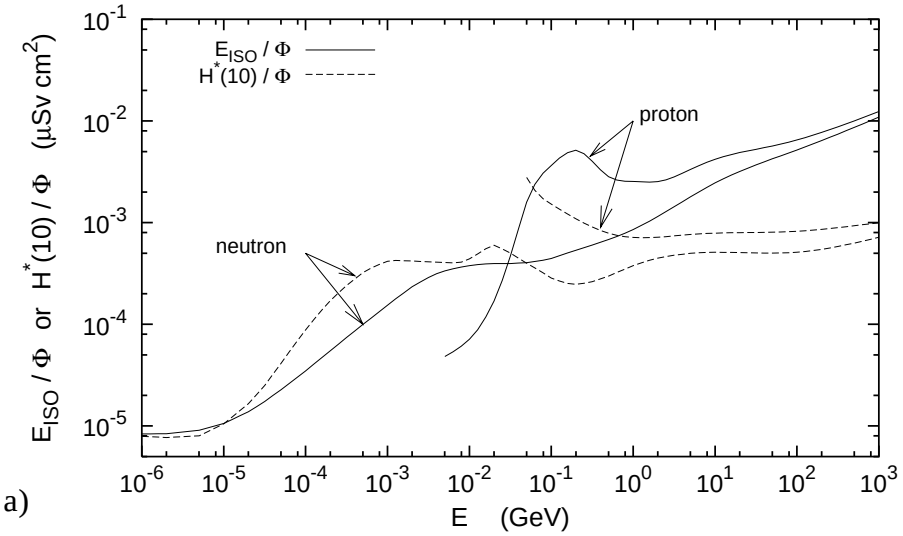

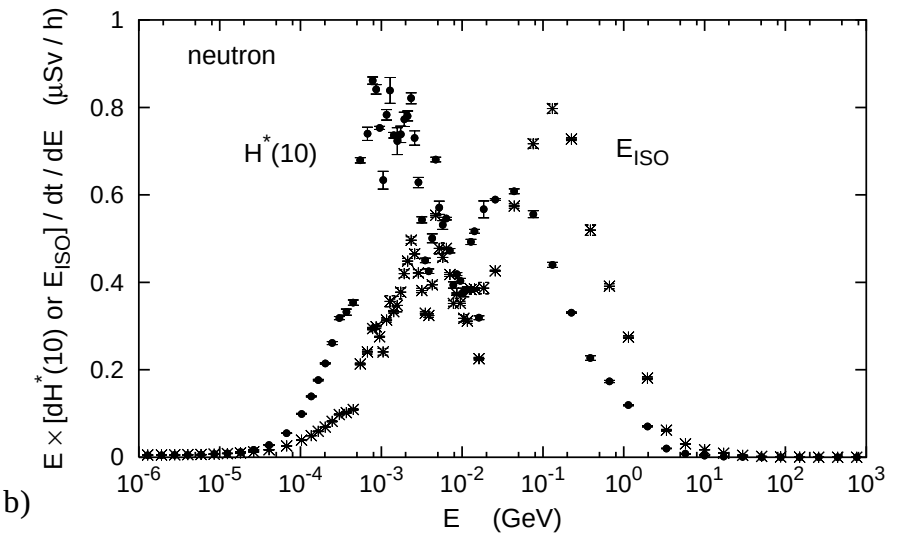

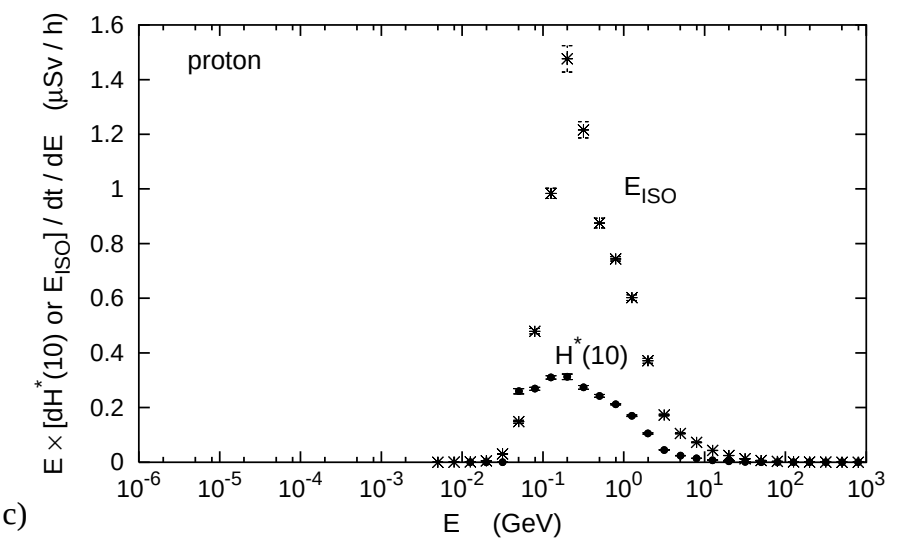

Figure 16: a) Conversion coefficients from fluence to effective dose (isotropic irradiation) and to ambient dose equivalent for neutrons and protons [56]. The coefficients for effective dose are based on the radiation weighting factors recommended in [57]. b) Effective dose and ambient dose equivalent spectra for neutrons and c) for protons obtained by folding the fluence spectra of Fig. 15 with the coefficients shown in a).

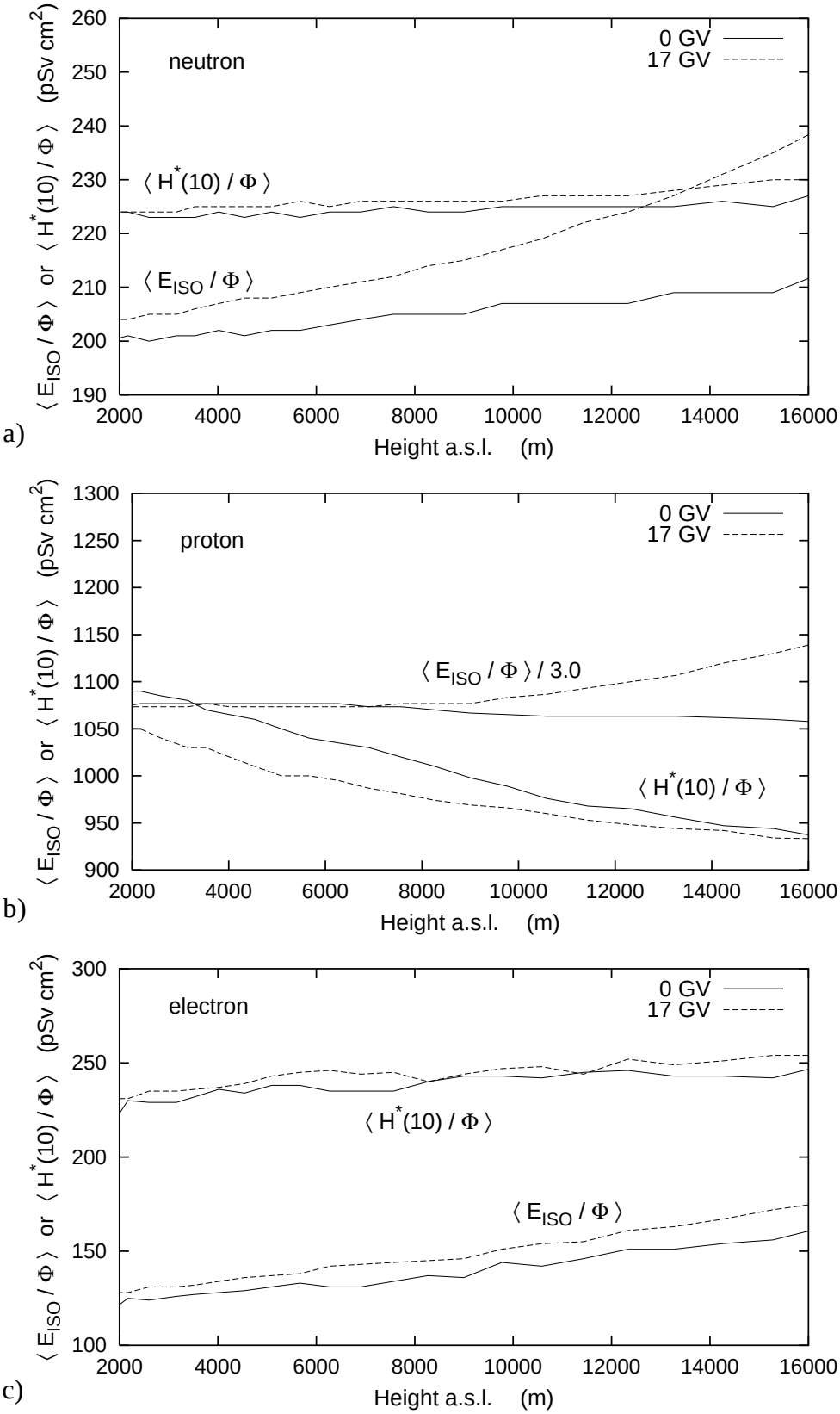

Figure 17: Average conversion coefficients from fluence to effective dose and ambient dose equivalent for a) neutrons, b) protons, and c) electrons / positrons as function of the height above sea level. The values are for solar minimum (465 MV) and are shown for zero rigidity cutoff (solid lines) and for a cutoff of 17 GV (dashed lines). The proton conversion coefficients for effective dose were scaled down by a factor of 3.

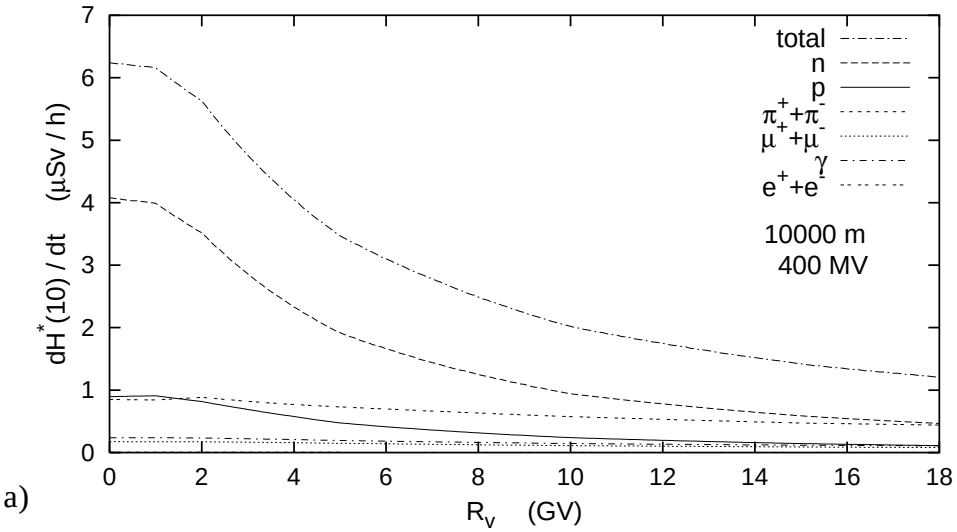

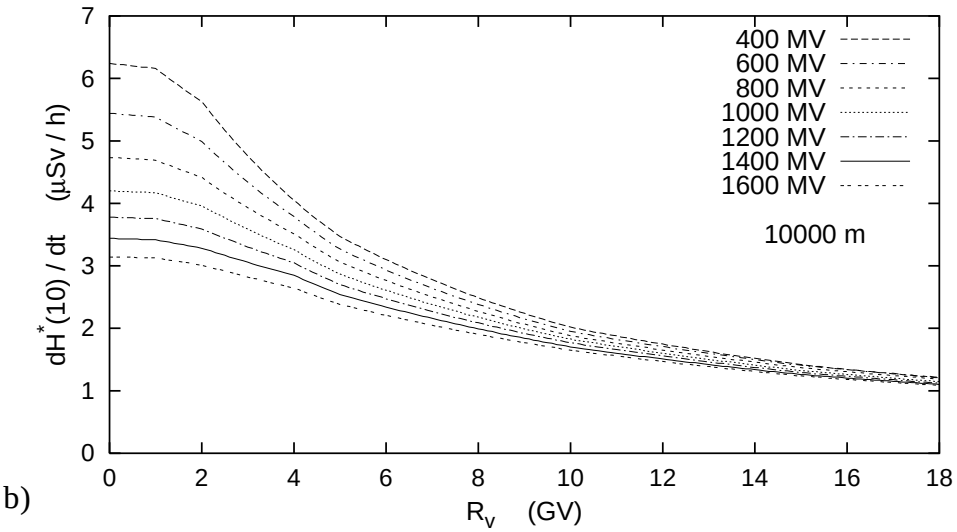

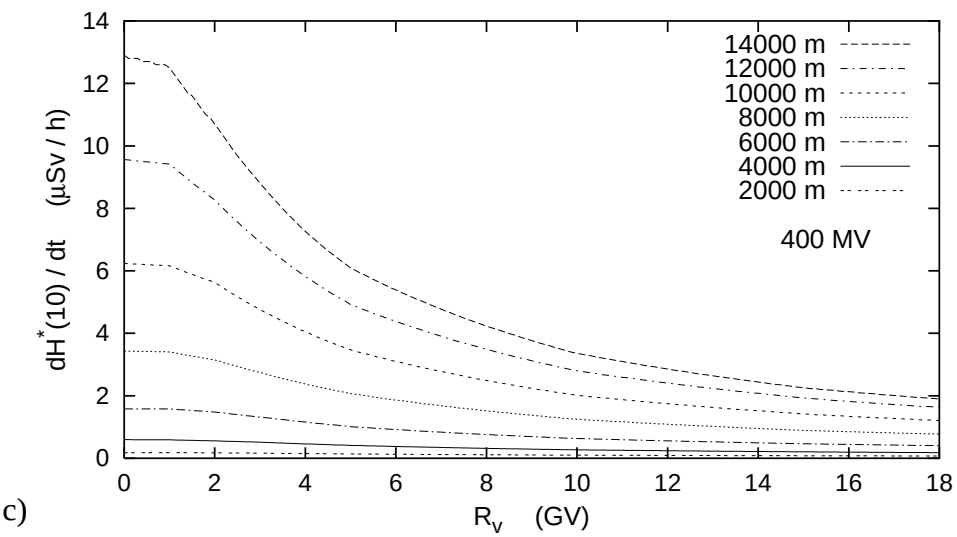

Figure 18: Ambient dose equivalent rate as function of the vertical rigidity cutoff of the primary particle spectrum for a) different types of particles at 10000 m above sea level and a solar modulation of 400 MV, b) different solar modulation parameters and a height above sea level of 10000 m, and c) different heights above sea level and a solar modulation of 400 MV. Figs. b) and c) show the total ambient dose equivalent rate.

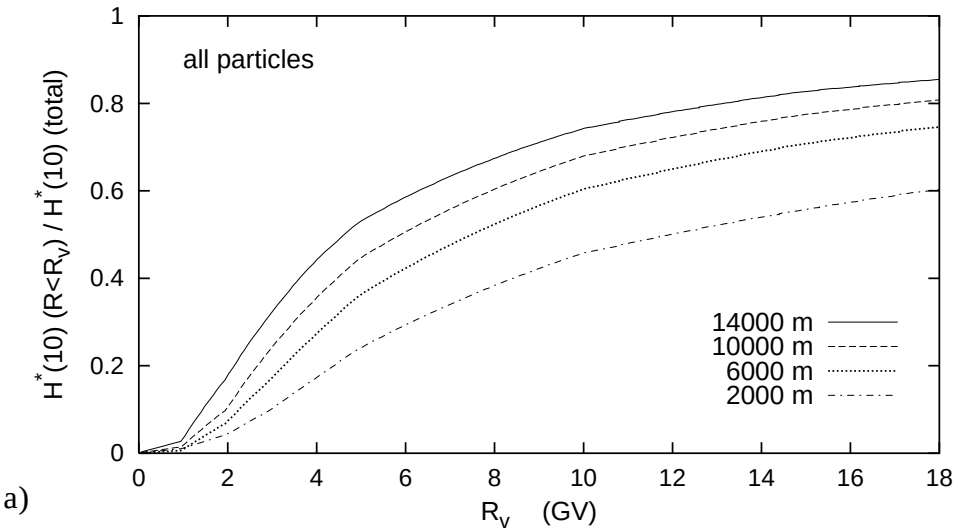

a)

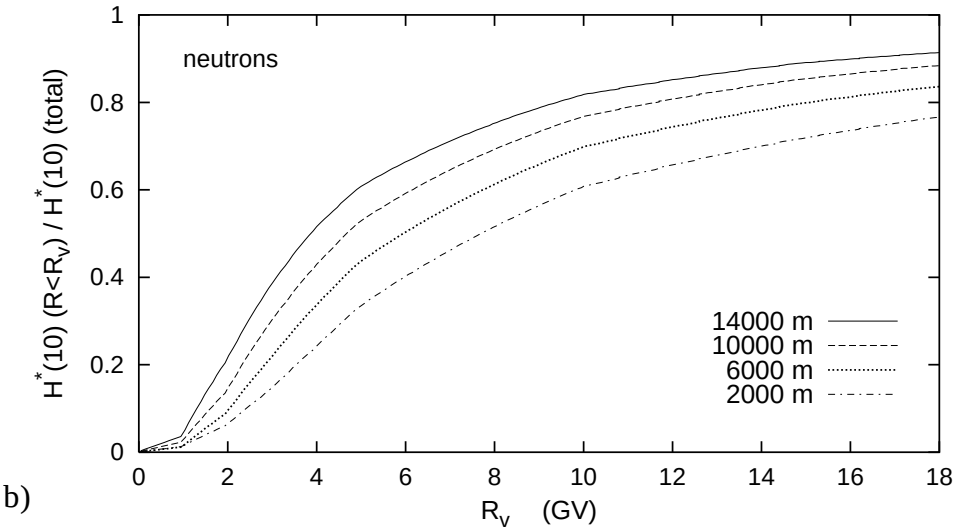

b)

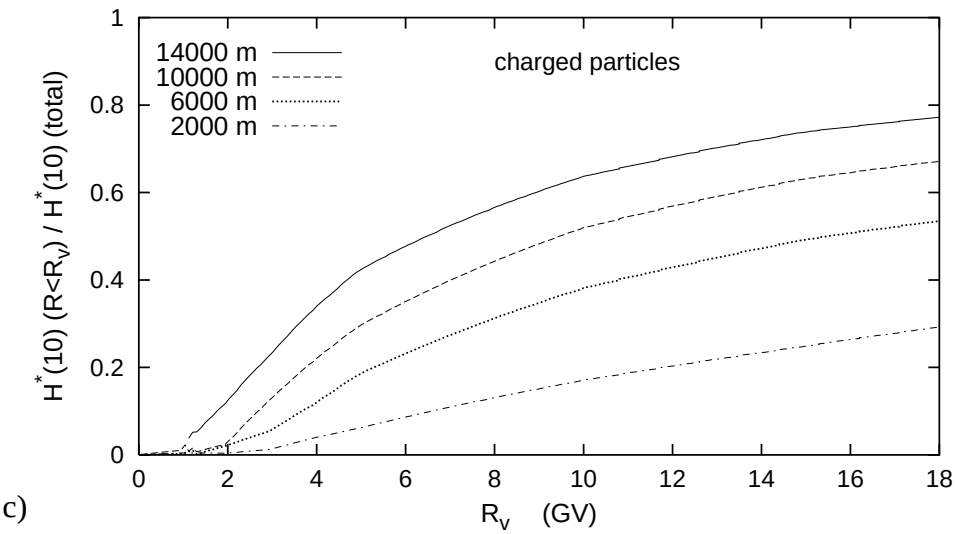

c)

Figure 19: Contribution of primary cosmic ray particles with a rigidity $R < R_{\rm v}$ to the ambient dose equivalent by a) all particles, b) neutrons, and c) charged particles at the geomagnetic pol as function of $R_{\rm v}$. The results are shown for four different heights above sea level and a solar modulation of $\Phi = 400$ MV.

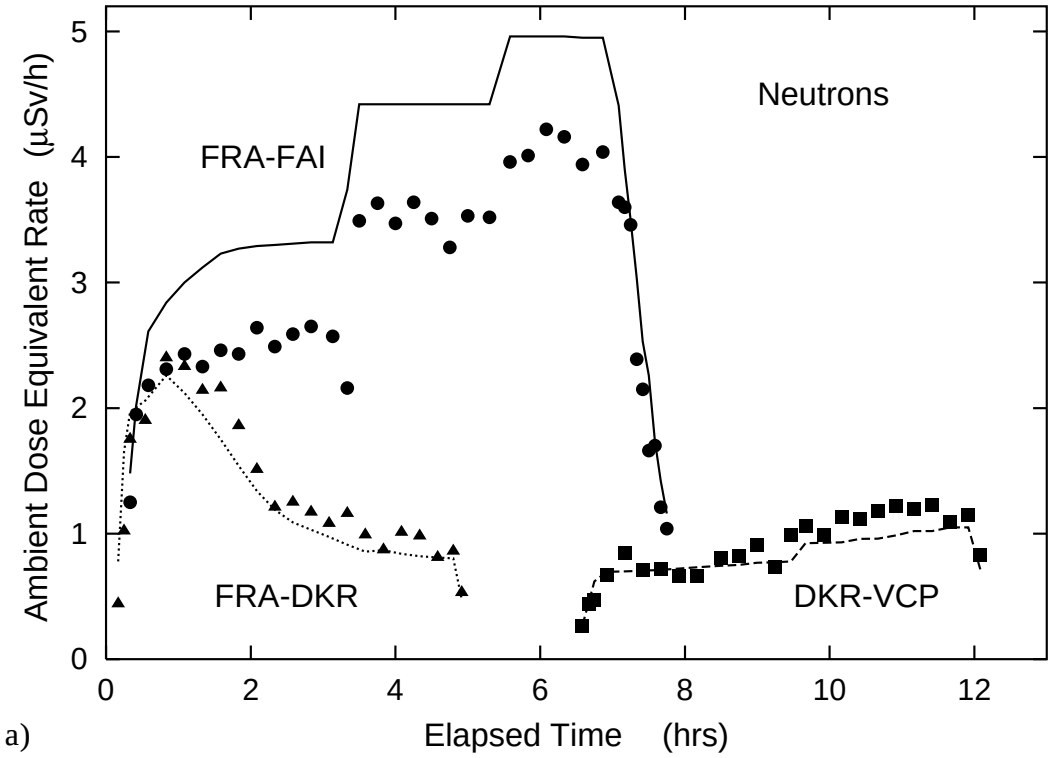

a)

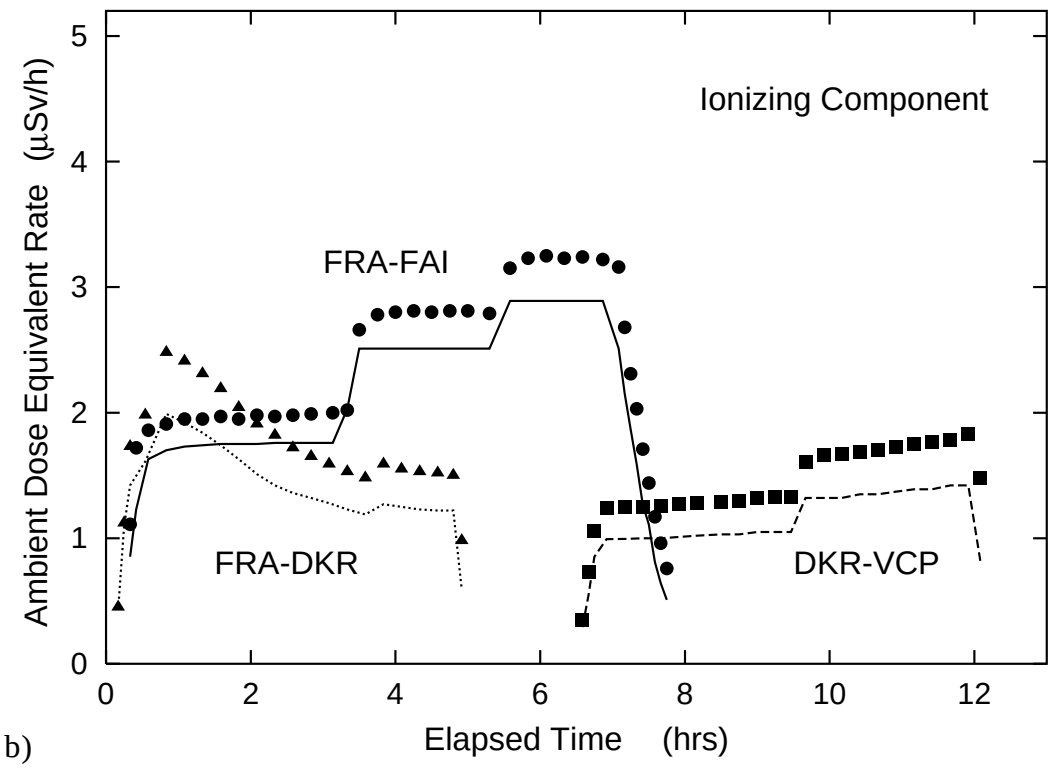

b)

Figure 20: Comparison of measured [58] and calculated ambient dose equivalent rate from (a) neutrons and (b) directly ionizing particles and photons (ionizing component) for two commercial flights, Frankfurt-Fairbanks (FRA-FAI) and Frankfurt-Sao Paulo with stopover in Dakar (FRA-DKR and DKR-VCP). The neutron dose was measured with a lead-modified Andersson and Braun rem-counter and the dose of the ionizing component with an ionization chamber. Doses are given as function of time after take-off.

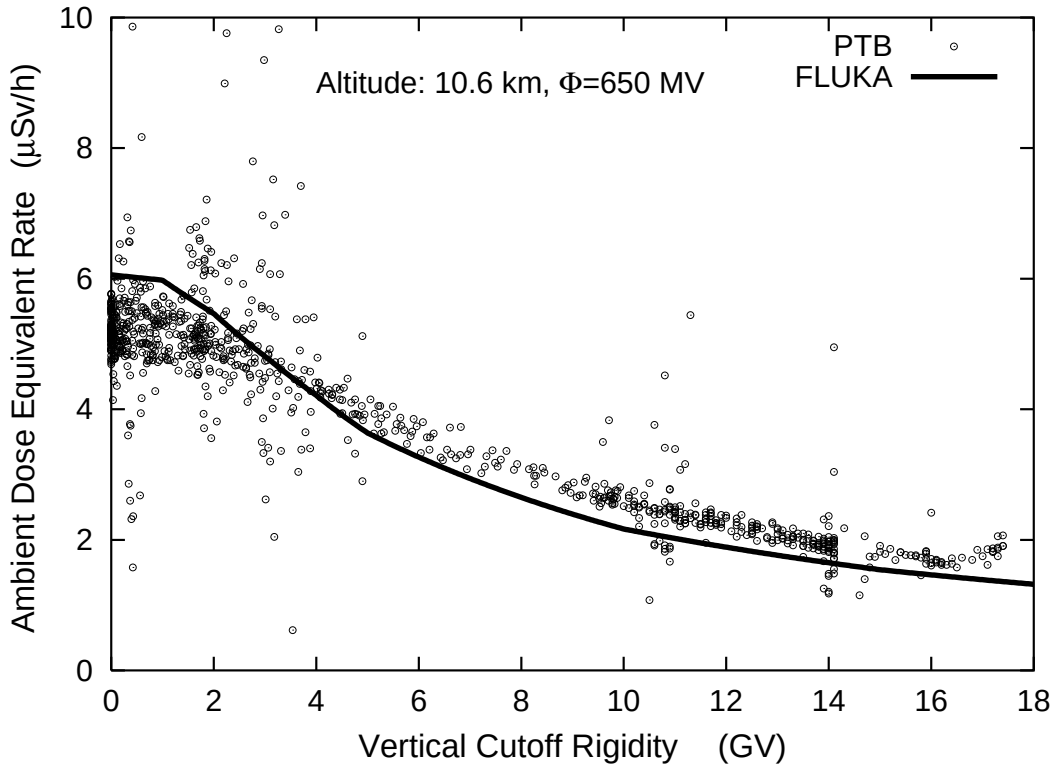

Figure 21: Total ambient dose equivalent rate measured aboard of cargo aircrafts [58] and as calculated with FLUKA The doses are shown as function of the vertical cutoff rigidity. Experimental and theoretical results were normalized to the same altitude (10.6 km) and solar modulation condition (650 MV) using calculated dependences.

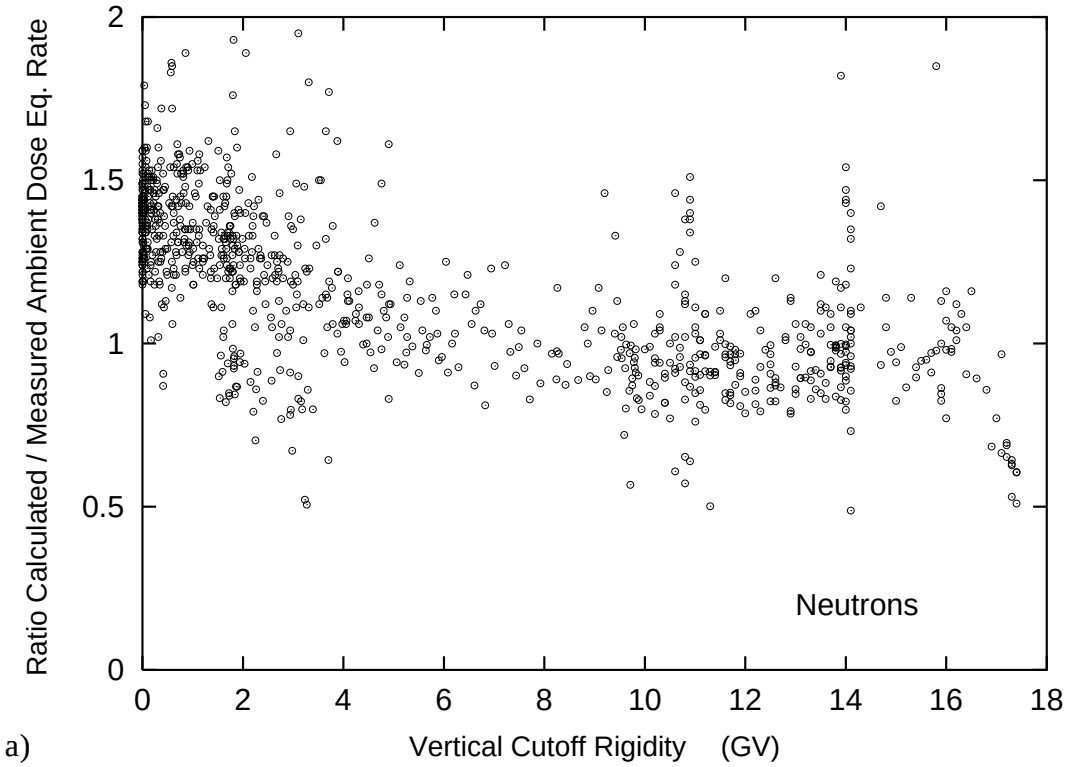

a)

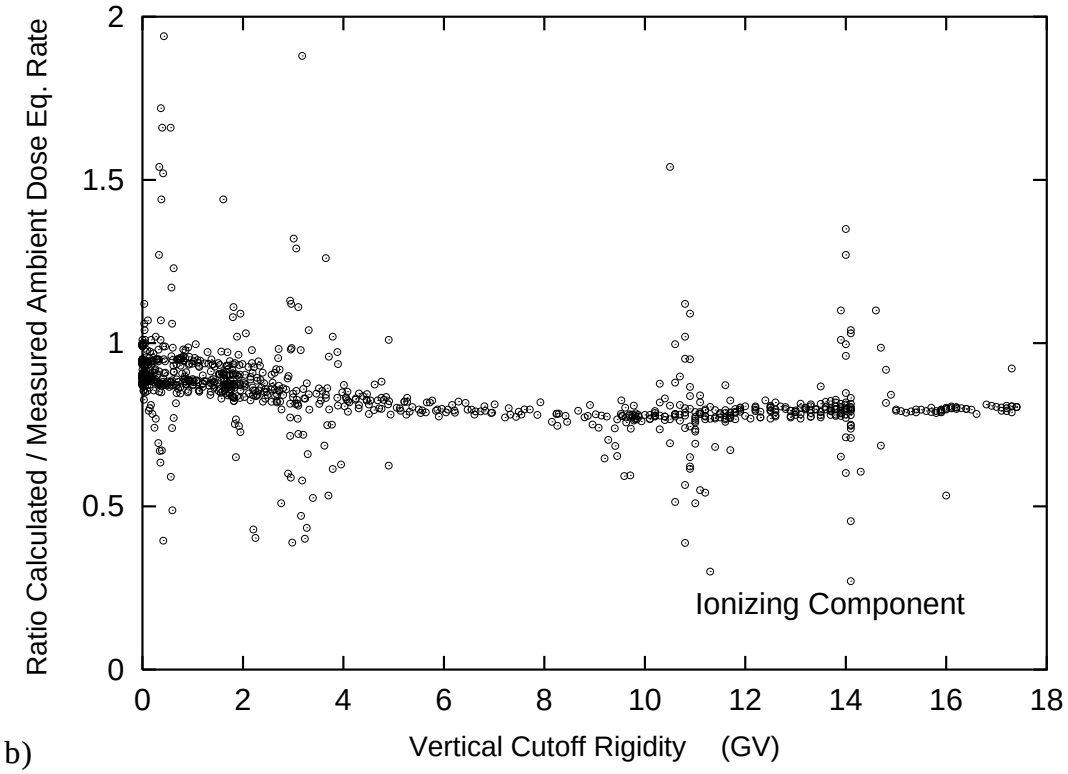

b)

Figure 22: Ratio of calculated and measured ambient dose equivalent (PTB measurements [58]) as function of the vertical cutoff rigidity. The ratios are shown for (a) dose from neutrons and (b) from directly ionizing particles and photons.

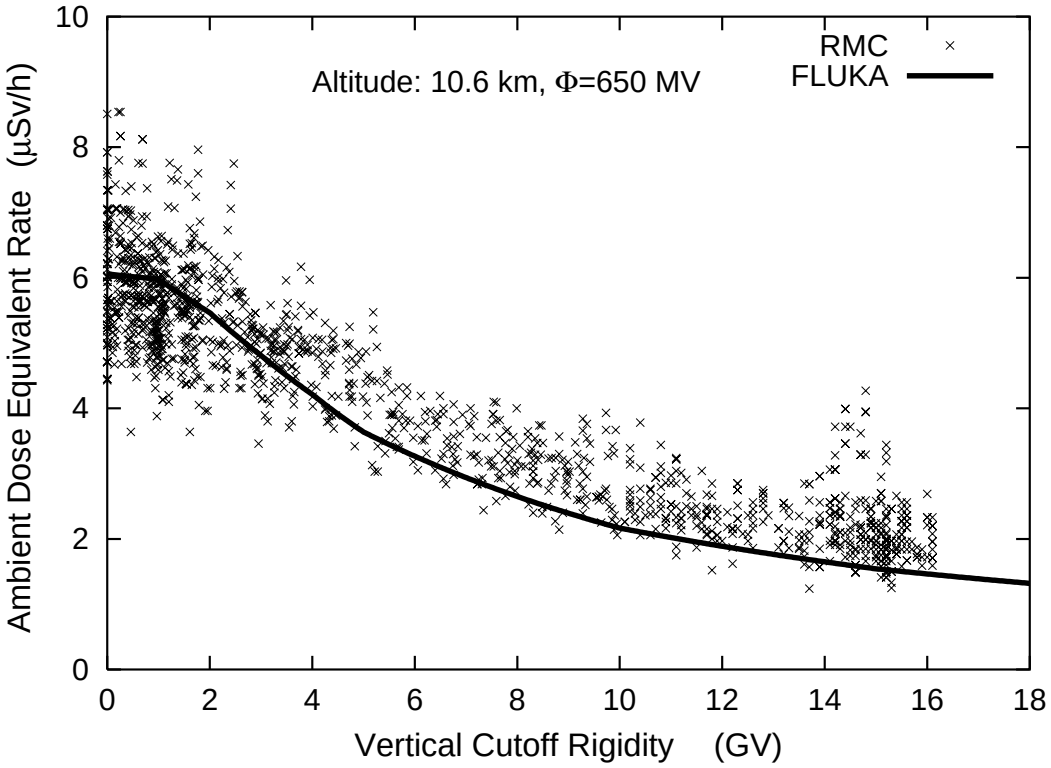

Figure 23: As in Fig. 21, here comparison with the RMC-data [60].

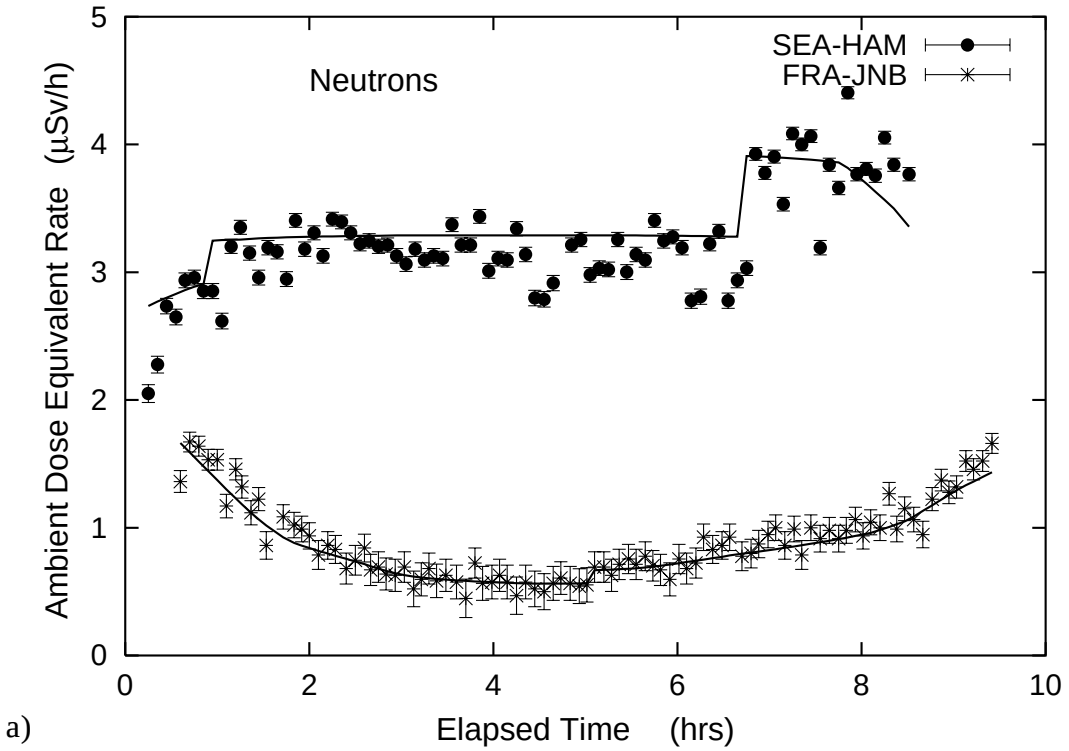

a)

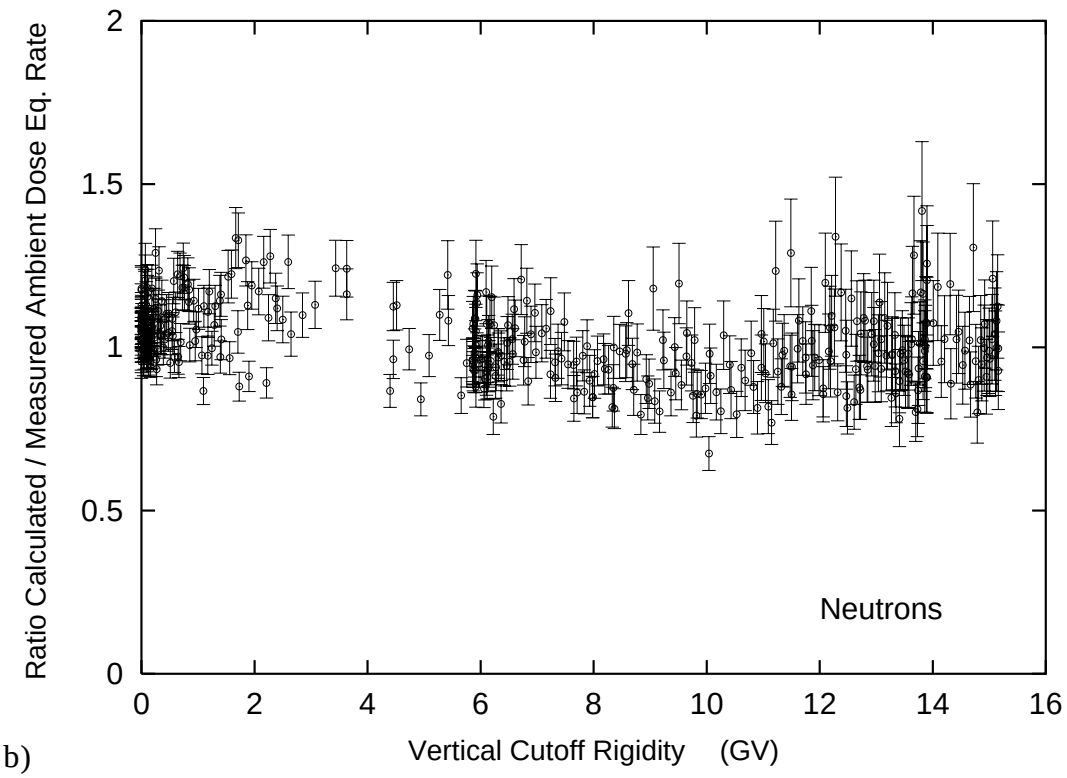

b)

Figure 24: (a) Comparison of ambient dose equivalent from neutrons measured during solar maximum on commercial flights from Seattle to Hamburg (SEA-HAM) and from Frankfurt to Johannesburg (FRA-JNB) with an Andersson-Braun rem counter with a lead-converter [62] and as calculated with FLUKA. Results are shown as function of the elapsed time after take-off. (b) Ratio of calculated and measured dose values for the same two flights and three further flights as function of the vertical rigidity cutoff. The error bars indicate the statistical counting errors of the experimental data.

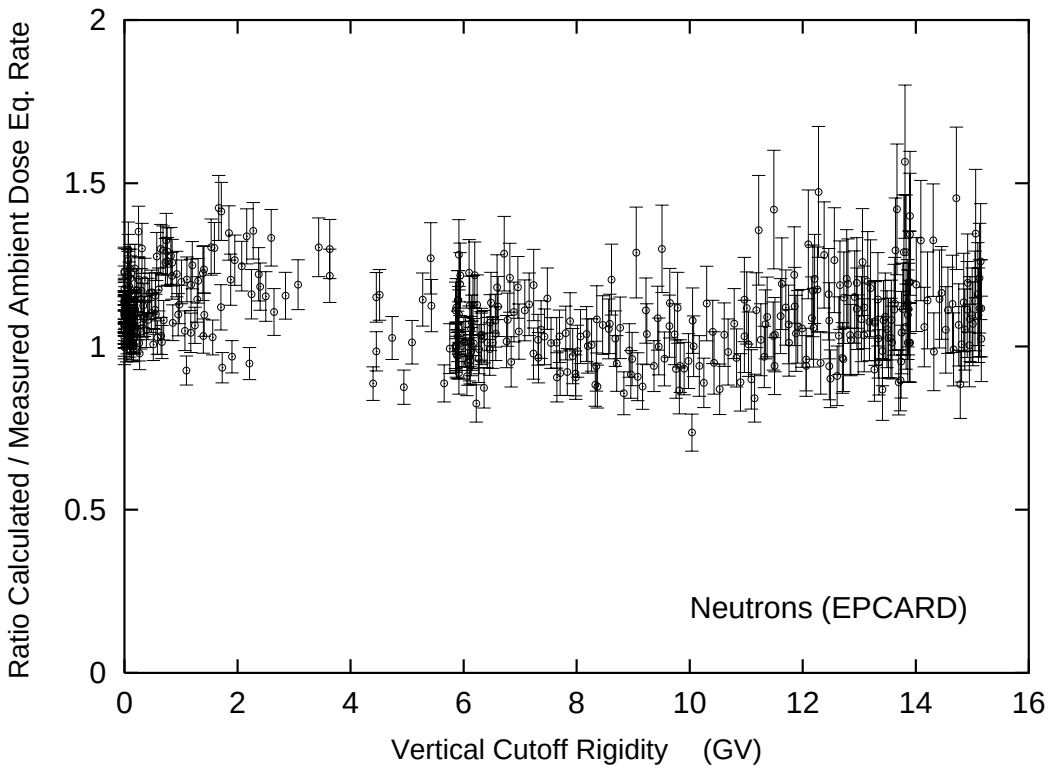

Figure 25: As in Fig. 24b, here shown for the predictions of EPCARD which is based on an earlier version of the FLUKA calculations.

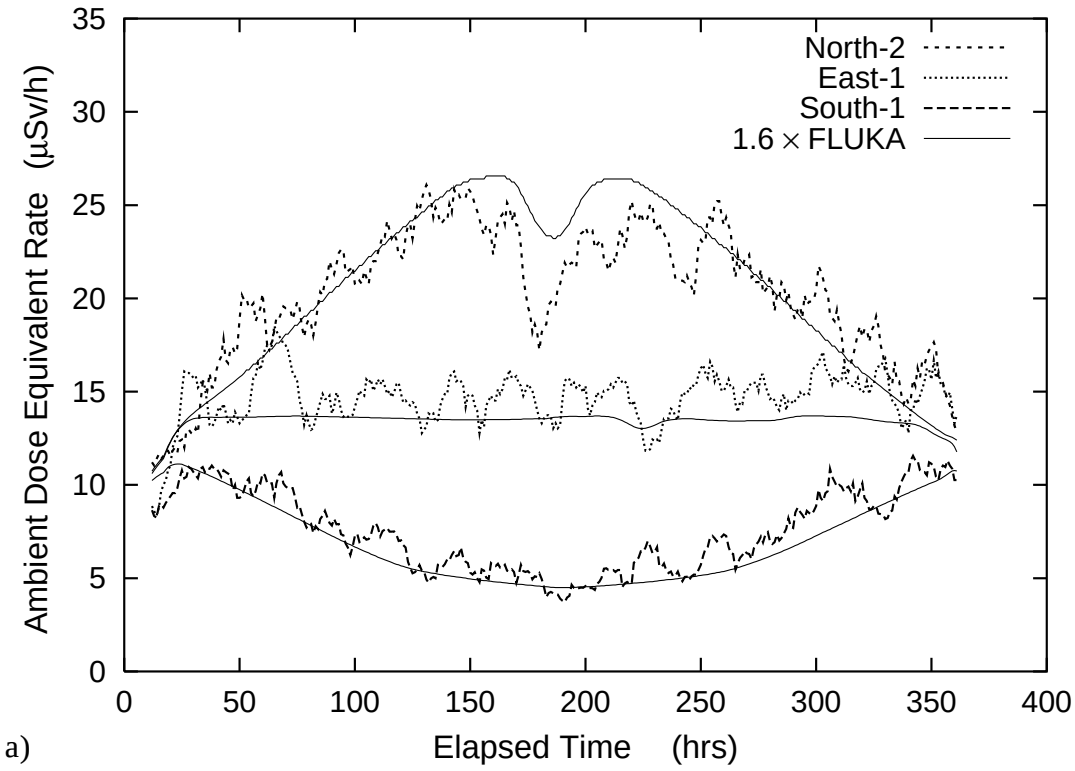

a)

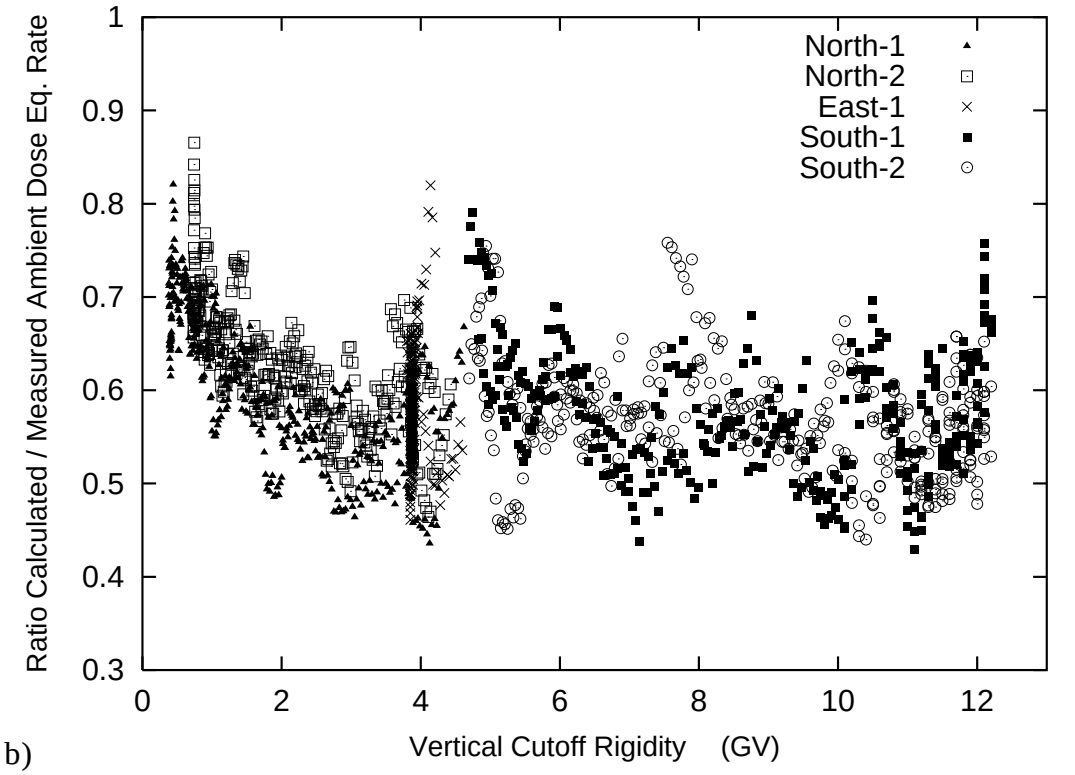

b)

Figure 26: Ambient dose equivalent rate at supersonic altitudes. (a) FLUKA results (solid lines) are compared to TEPC data measured aboard of an ER2 high-altitude airplane [63, 64]. The experimental data were divided by a factor of 1.15 in order to account for a calibration discrepancy [64]. In addition, the FLUKA results were multiplied by a factor of 1.6 in order to allow a direct comparison of the dose rate as function of the elapsed time after take-off. The comparison is shown for three selected flights. (b) Ratio of the calculated and measured ambient dose equivalent rate as function of the vertical rigidity cutoff for all five flights.